

AD-A238 839



## REPORT DOCUMENTATION PAGE

2

Unclassified			1b. RESTRICTIVE MARKINGS	
2a. SECURITY CLASSIFICATION AUTHORITY			3. DISTRIBUTION / AVAILABILITY OF REPORT	
2b. DECLASSIFICATION / DOWNGRADING SCHEDULE			Approved for public release; distribution unlimited	
4. PERFORMING ORGANIZATION REPORT NUMBER(S) Final Report			5. MONITORING ORGANIZATION REPORT NUMBER(S) N00014-87-K-0531	
6a. NAME OF PERFORMING ORGANIZATION University of California, Los Angeles/ Bruce Dunn		6b. OFFICE SYMBOL (if applicable)		7a. NAME OF MONITORING ORGANIZATION Office of Naval Research- Dr. R. Schwartz
6c. ADDRESS (City, State, and ZIP Code) Dept. of Materials Science & Engineering University of California, Los Angeles / 90024-1595			7b. ADDRESS (City, State, and ZIP Code) Naval Weapons Center China Lake, CA 93555	
8a. NAME OF FUNDING / SPONSORING ORGANIZATION		8b. OFFICE SYMBOL (if applicable)		9. PROCUREMENT INSTRUMENT IDENTIFICATION NUMBER
8c. ADDRESS (City, State and ZIP Code)			10. SOURCE OF FUNDING NUMBERS	
			PROGRAM ELEMENT NO	PROJECT NO
			TASK NO	WORK UNIT NO
11. TITLE (Include Security Classification) Precipitation Haraening of Infrared Transmitting ZnS Ceramics				
12. PERSONAL AUTHOR(S) Bruce Dunn and Alan Ardell				
13a. TYPE OF REPORT Technical - Final		13b. TIME COVERED FROM May 1987 TO Oct. 1990		14. DATE OF REPORT (Year, Month, Day) 1991, June 30
15. PAGE COUNT 4 + Appendix				
16. SUPPLEMENTARY NOTATION				
17. COSATI CODES			18. SUBJECT TERMS (Continue on reverse if necessary and identify by block number)	
FIELD	GROUP	SUB-GROUP		
19. ABSTRACT (Continue on reverse if necessary and identify by block number)				
Final Report of Contract N00014-87-K-0531				
91 8 05 009				
91-06835				
20. DISTRIBUTION / AVAILABILITY OF ABSTRACT <input checked="" type="checkbox"/> UNCLASSIFIED/UNLIMITED <input type="checkbox"/> SAME AS RPT <input type="checkbox"/> DTIC USERS			21. ABSTRACT SECURITY CLASSIFICATION Unclassified	
22a. NAME OF RESPONSIBLE INDIVIDUAL			22b. TELEPHONE (Include Area Code)	22c. OFFICE SYMBOL

**FINAL REPORT**

**Contract No. N00014-87-K-0531**

Precipitation Hardening of Infrared Transmitting ZnS Ceramics

Principal Investigators: B. Dunn and A. J. Ardell

Department of Materials Science and Engineering  
University of California, Los Angeles  
Los Angeles, CA 90024-1595

A-1

## **A. Scientific Research Goals**

Precipitation strengthening is a potentially attractive technique for hardening and toughening infrared transmitting materials. The controlled precipitation of a finely dispersed second phase offers the opportunity to improve mechanical properties without degrading optical properties. It is well established that the presence of an appropriate dispersion of second phase particles can improve the mechanical behavior of ceramics, and, by maintaining a particle size  $<100$  nm, scattering losses in the infrared will be low and the need to index-match the ZnS matrix with the second phase will be circumvented.

The overall objectives of the research program have been (1) to demonstrate that ZnS-based ceramics can be precipitation-strengthened and (2) to characterize the resulting mechanical and optical properties of the multiphase materials. An important research goal has been to identify ZnS-based systems suitable for strengthening and to determine the composition ranges and annealing treatments required to produce precipitate phases or other solid-state reaction products. Another important research objective has been to determine why "alloys" in the ZnS- $\text{Ga}_2\text{S}_3$  system exhibit an increase in both fracture toughness and hardness, and to establish the composition ranges and annealing treatments which produce this behavior. The research has also sought to quantify the effects of size and volume fraction of various second phase constituents on infrared scattering. The relationship between mechanical behavior and microstructural development has been of central importance in this research program.

## **B. Summary of Research Accomplishments**

Candidate systems for precipitation strengthening have been identified, i.e., the ZnS-CdS and ZnS-ZnGa<sub>2</sub>S<sub>4</sub> systems. The phase equilibria in the ZnS-rich region of these two systems have been established. CdS is very soluble in ZnS and the two-phase microstructure envisioned in this system will consist of sphalerite and wurtzite solid solutions.  $\text{Ga}_2\text{S}_3$  exhibits limited solubility in ZnS and the pseudobinary ZnS-ZnGa<sub>2</sub>S<sub>4</sub> system is characterized by a eutectoid reaction. The equilibrium phase diagrams for both systems were published and are attached to this report.

The research program focussed on the ZnS-ZnGa<sub>2</sub>S<sub>4</sub> system. We developed hot pressing methods for ZnS and ZnS-Ga<sub>2</sub>S<sub>3</sub> "alloys" which routinely produced samples exceeding 99.0% of their theoretical density. These high quality specimens were used to characterize mechanical and optical properties of materials containing 8 to 16 mol% Ga<sub>2</sub>S<sub>3</sub>.

The most significant result obtained during the program was the observation that the various ZnS-Ga<sub>2</sub>S<sub>3</sub> compositions exhibit considerably higher fracture toughness and hardness than pure ZnS. The increase in hardness was proportional to the amount of Ga<sub>2</sub>S<sub>3</sub> added, with the 16 mol% sample exhibiting a value nearly two times larger than ZnS. A sizeable increase in fracture toughness was also observed in all samples. At 12 mol% Ga<sub>2</sub>S<sub>3</sub>, the fracture toughness value was more than 50% greater than that of pure ZnS. In these studies, all samples were solid-solution treated in the wurtzite phase (at 940°C), and no precipitated phases were detected by x-ray diffraction. The mechanism responsible for the observed increase in hardness and fracture toughness has yet to be determined. The publication describing these results is attached to the report.

The optical properties of several ZnS-Ga<sub>2</sub>S<sub>3</sub> solid solutions have been measured. As expected, the infrared transmission exhibited no change from that observed for pure ZnS, with excellent transmission until the infrared cut-off in the 12  $\mu$ m range. In addition to this experimental work, a model has been derived which enables us to calculate the scattering efficiency factor as a function of wavelength for a multiphase material with a given particle size and refractive index for the second phase. By applying this model to pure ZnS (where pores constitute the second phase), we were able to make a unique calculation of the pore size distribution in the ceramic by measuring the optical transmission. A manuscript describing the model is attached to this report.

Another significant result is the successful development of a method for measuring fracture toughness using an indented miniaturized ring-on-ring disk-bend fracture toughness test (MDBFTT). Samples 3 mm in diameter and 300 to 400  $\mu$ m thick are indented using a Vickers indenter and the load to fracture is measured in the MDBFTT. This is repeated for several loads, after which already developed fracture toughness equations are applied to the data, yielding a value of  $K_{Ic}$ . The fracture toughness can be obtained by this method without measuring actual crack lengths, thereby

eliminating the uncertainties associated with such measurements. Initial measurements on standard samples, including CVD-grown ZnS, have yielded values which are in excellent agreement with conventional fracture toughness measurements. The attached manuscript provides full details of the technique and the results to date.

## Solid-State Phase Equilibria in the ZnS-Ga<sub>2</sub>S<sub>3</sub> System

Jimin Zhang,\* William W. Chen, Alan J. Ardell, and Bruce Dunn\*

Department of Materials Science and Engineering, University of California,  
Los Angeles, California 90024

The ZnS-Ga<sub>2</sub>S<sub>3</sub> equilibrium phase diagram has been determined to 50 mol% over the temperature range 700° to 900°C. Samples of various compositions were prepared via solid-state diffusion starting from powders of the pure components. The identification of the phases was determined by X-ray diffraction methods. The principal feature of the phase equilibria is the eutectoid transformation at 818 ± 5°C of hexagonal wurtzite containing 16 ± 1 mol% Ga<sub>2</sub>S<sub>3</sub> to cubic ZnS and tetragonal ZnGa<sub>2</sub>S<sub>4</sub>. ZnGa<sub>2</sub>S<sub>4</sub> is the equilibrium compound at 50 mol% Ga<sub>2</sub>S<sub>3</sub>, but it exists over a considerable range of stoichiometry. The solubility of Ga<sub>2</sub>S<sub>3</sub> in ZnS increases with increasing temperature to a maximum of 9 ± 1 mol% at the eutectoid temperature. [Key words: phase diagrams, zinc sulfide, solid state, wurtzite, eutectics.]

### I. Introduction

ZINC SULFIDE is commercially used as an infrared (IR) transmitting material because of its good optical transmission up to 12 μm and adequate mechanical strength. However, ZnS-based ceramics with improved fracture toughness, thermal-shock resistance, and erosion resistance are absolutely essential for certain IR-window applications. There are several possible approaches to attain the desired combination of improved mechanical properties while retaining IR transmittance comparable to that of ZnS. Our approach is to explore the possibilities of strengthening and toughening ZnS by the addition of dispersions of particles of a second phase, with the dispersoids introduced into the microstructure by the appropriate heat treatment of densified samples. The second-phase additions should also have intrinsically good IR transmittance and a closely matching refractive index in order to minimize optical attenuation losses due to scattering. This requirement places certain restrictions on the suitability of the ions added for alloying purposes.

To improve the mechanical behavior of ZnS through heat treatment, knowledge of solid-solid phase equilibria involving ZnS and other sulfides is also essential. Unfortunately, such data are limited, and we have had to undertake the task of determining some binary phase diagrams ourselves. Among the various possibilities we have considered, the ZnS-CdS and ZnS-Ga<sub>2</sub>S<sub>3</sub> systems appear to be especially promising for meeting all the requirements noted above. We have already reported the results of the determination of the ZnS-rich portion of the ZnS-CdS phase diagram<sup>1</sup> and have presented a preliminary version of the ZnS-Ga<sub>2</sub>S<sub>3</sub> phase diagram.<sup>2</sup> In this paper, we present the ZnS-Ga<sub>2</sub>S<sub>3</sub> phase diagram to 50 mol% Ga<sub>2</sub>S<sub>3</sub> at the same time refining the earlier version.

The first study of this phase diagram was made by Gates and Edwards,<sup>3</sup> using the simultaneous Knudsen and dynamic

torsion-effusion method. They published the Ga<sub>2</sub>S<sub>3</sub>-rich end of the partial ZnS-Ga<sub>2</sub>S<sub>3</sub> phase diagram, locating the phase boundaries to within ±15°C. However, this part of the diagram is of no interest for strengthening ZnS-based ceramics. Malevskii<sup>4</sup> studied the ZnS-Ga<sub>2</sub>S<sub>3</sub> system using the solid-state reaction technique and published a partial phase diagram at the ZnS-rich end. His work has established that the solubility of Ga<sub>2</sub>S<sub>3</sub> increases with increasing temperature and that the diagram contains a eutectoid reaction around 800°C. The eutectoid reaction reported involved the composition of wurtzite containing approximately 20 mol% Ga<sub>2</sub>S<sub>3</sub> to form sphalerite and the thiogallate phase ZnGa<sub>2</sub>S<sub>4</sub>, containing approximately 14 and 28 mol% Ga<sub>2</sub>S<sub>3</sub>, respectively.

ZnGa<sub>2</sub>S<sub>4</sub> itself is a good IR-transmitting material in the range 2.5 to 12 μm and has the *I42m* tetragonal crystal structure.<sup>5,6</sup> The tetragonal unit cell has lattice parameters *a*<sub>1</sub> and *c*<sub>1</sub> of 0.5297 and 1.0363 nm, respectively.<sup>6</sup> The lattice mismatch with cubic sphalerite ZnS (*a*<sub>2</sub> = 0.5410 nm) is very small, which probably accounts for the fairly large solubility of thiogallate in sphalerite (despite the difference in valence between Zn and Ga) reported by Malevskii. Also, the microhardness of ZnGa<sub>2</sub>S<sub>4</sub> has been found to be close in value to that of ZnS.<sup>7</sup>

Based on the factors discussed above, it is clear that Ga<sub>2</sub>S<sub>3</sub> satisfies the requirements for a suitable second-phase addition. ZnS-rich solid solutions should be precipitation hardenable, whereas alloys of near eutectoid composition offer the prospect of microstructural manipulation by eutectoid decomposition. Additionally, the expected decomposition product, ZnGa<sub>2</sub>S<sub>4</sub>, is optically compatible with ZnS. One of the major drawbacks to the development of these "alloys" as IR materials is the accuracy of Malevskii's phase diagram, because the compositions of the samples used in his investigation differed by as much as 10 mol%. This was the main reason for undertaking the current investigation.

### II. Experimental Procedure

X-ray diffraction was the principal technique employed to investigate the phase equilibria. Powders of ZnS (99.9%)<sup>8</sup> and Ga<sub>2</sub>S<sub>3</sub> (99.99%)<sup>9</sup> were used as starting materials for the preparation of alloys by solid-state reaction. The method of preparation used in the present study was previously described by Chen *et al.*<sup>1</sup> The powders were mixed, ground with a mortar and pestle, sealed under vacuum in a fused silica ampule, and heated to the reaction temperature. Independent chemical analyses were not performed on the reacted powders, so the concentrations reported are those derived from the original measurements of the weighed powders. The accuracy of these measurements is ±0.5%.

In order to assure that equilibrium was attained, the reaction times were chosen so that the lattice constants of the solid solutions no longer changed as the reaction time increased. A solid-state reaction period of more than 10 weeks was necessary at 700°C, but shorter times were used at the

W. White—contributing editor

Manuscript No. 198134. Received September 6, 1989; approved January 22, 1990.

Supported by the Office of Naval Research under Contract No. N00014-82-K-0531.

\*Member, American Ceramic Society.

<sup>8</sup>Aesar, Seabrook, NH  
<sup>9</sup>Alfa, Ward Hill, MA

higher reaction temperatures. The ampules were quenched into water at room temperature after all reaction treatments. The various conditions are summarized in Table I. The intervals in composition of the samples were 1 or 2 mol% near the phase boundaries and 3 or 5 mol% elsewhere. We have found that the approach to equilibrium is far faster for the mixed powders than for compacted samples of identical composition. This is because the eutectoid decomposition reaction is very sluggish.

The parametric method<sup>8</sup> and a modified version of the disappearing-phase method<sup>8,9</sup> were used to establish the solvus compositions. The choice of method was determined by the crystal structures of the equilibrium phases present. In particular, the X-ray diffraction peaks of wurtzite are readily distinguished from those of the sphalerite and thiogallate phases. However, the sphalerite and thiogallate phases are structurally similar, and many of their peaks overlap. For this reason, the disappearing-phase method was used to determine the phase boundaries at 850° and 900°C, where wurtzite is in equilibrium with either sphalerite or thiogallate, depending on composition. The parametric method was used to establish the phase boundaries between the low-temperature sphalerite and thiogallate phases.

The parametric method takes advantage of the variation of the lattice constants with solute concentration in solid solutions. It is a classical technique which is thoroughly described by Cullity,<sup>8</sup> and requires no further discussion except to note that NaCl powder (99.98%)<sup>†</sup> was mixed with the reacted samples for use as an internal standard in the X-ray diffraction analysis. Ni-filtered CuK $\alpha$  X-rays were employed, with the diffractometer operating in a digital step-scanning mode (0.01° for 10 or 20 s).

The basis of the disappearing-phase method is that the fraction of a particular phase present in the alloy is proportional to the integrated intensity,  $I$ , of one of its X-ray peaks. Klug and Alexander<sup>9</sup> have shown that in a two-phase mixture of, say, the wurtzite (w) and thiogallate (t) phases, the X-ray intensity of wurtzite can be expressed as

$$\frac{I_w}{I_{wp}} = \frac{X_w \mu_w}{X_w(\mu_w - \mu_t) + \mu_t} = \frac{X_w \mu_w}{X_w \mu_w + X_t \mu_t} \quad (1)$$

where  $I_w$  is the intensity of a specific wurtzite peak in the two-phase mixture,  $I_{wp}$  is the intensity of the same peak, but when the material is 100% wurtzite containing its equilibrium concentration of Ga<sub>2</sub>S<sub>3</sub> (this is *not* pure wurtzite), the  $\mu$ 's are mass absorption coefficients of the two phases at their equilibrium concentrations of Ga<sub>2</sub>S<sub>3</sub>, and the  $X$ 's are the fractions by weight of the two phases.

Equation (1) is not in an especially useful form because  $I_{wp}$  is difficult to measure (measurement of  $I_{wp}$  requires the preparation of wurtzite containing its equilibrium concentration of Ga<sub>2</sub>S<sub>3</sub> at a particular temperature, which is precisely what we are trying to determine). To transform it into a useful equation, we first write it as

$$\frac{I_w}{I_w + I_t} = \frac{I_{wp} X_w \mu_w}{I_{wp} X_w \mu_w + I_{tp} X_t \mu_t} \quad (2)$$

<sup>†</sup>Fisher, Pittsburgh, PA.

Table I. Solid-State Reaction Conditions

T (°C)	Time (h)
700	1700
750	550
800	1400
850	910
900	385

which makes use of the counterpart of Eq. (1) written for the thiogallate phase instead. We then apply the lever rule, i.e.

$$X_w = \frac{W_t - W_0}{W_t - W_w} \quad X_t = \frac{W_0 - W_w}{W_t - W_w}$$

where  $W_0$  is the weight fraction of Ga<sub>2</sub>S<sub>3</sub> in the sample, and  $W_w$  and  $W_t$  are the equilibrium weight fractions of Ga<sub>2</sub>S<sub>3</sub> in the wurtzite and thiogallate phases, respectively. Substitution of these into Eq. (2) produces the result

$$\frac{I_w}{I_w + I_t} = \frac{W_t - W_0}{W_t - W_0 + \frac{I_{tp} \mu_t}{I_{wp} \mu_w} (W_0 - W_w)} \quad (3)$$

Since the ratio  $I_{tp} \mu_t / I_{wp} \mu_w$  is constant within the two-phase W + T region at any specific temperature, and  $W_w < W_0 < W_t$ , the ratio  $I_w / (I_w + I_t)$  clearly varies between 0 and 1 as the equilibrium solvus compositions are approached. If  $I_{tp} \mu_t / I_{wp} \mu_w$  were equal to unity,  $I_w / (I_w + I_t)$  would be equal to  $X_w$  and its variation with  $W_0$  would be linear. Such is not generally the case, however, which introduces curvature into such plots even if the diffraction peaks chosen are nearly equally intense when the relative proportions of the two phases are approximately equal (i.e., when  $X_w \approx X_t \approx 0.5$ ).

In the application of Eq. (3) to our experimental data, the {331} sphalerite peak, the {0002}, {2023}, {2130}, and {2131} wurtzite peaks, and the {112}, {316}, and {413} thiogallate peaks were used for the intensity measurements. The integrated intensities were calculated using the pow computer program.<sup>10</sup> This program subtracts the K $\alpha_2$  component and calculates the integrated intensities with a relative error of less than 2%.

### III. Results and Discussion

#### (I) Phase Fields in the ZnS-ZnGa<sub>2</sub>S<sub>3</sub> Pseudobinary System

An analysis of the diffraction peaks identified the phases present in the sample. The results are plotted in Fig. 1, where the shaded regions indicate the positions of the phase boundaries consistent with the data. Preliminary examination revealed the existence of three different solid-solution phases, namely, sphalerite (S), wurtzite (W), and the tetragonal thiogallate (T) and three two-phase fields (S + W, W + T, and S + T). It is obvious that the wurtzite solid solution must undergo the eutectoid transformation  $W \rightarrow S + T$ , but the eutectoid temperature and composition cannot be determined accurately from the information in Fig. 1. All of these general features were noted by Malevskii,<sup>4</sup> although his diagram is inconsistent with the data in Fig. 1.

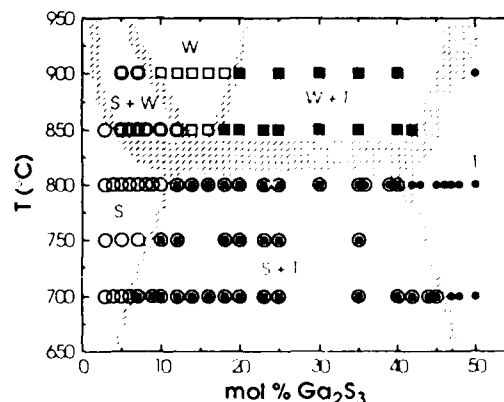


Fig. 1. Phase map of the ZnS-Ga<sub>2</sub>S<sub>3</sub> system to 50 mol%. The shaded regions show the most likely locations of the phase boundaries. The open circles indicate the presence of sphalerite (S), the open squares the presence of wurtzite (W), and the filled circles the presence of thiogallate (T).

## (2) Quantitative Evaluation of the Phase Boundaries

Figure 2 shows examples of the use of the disappearing-phase method used to determine the S/W and W/T solvi at two different temperatures. The intensity ratios  $I_s/(I_s + I_w)$  and  $I_w/(I_w + I_t)$  are plotted vs wt%  $\text{Ga}_2\text{S}_3$  for the S + W and W + T phase fields, respectively. The use of weight percent rather than mole percent was dictated by the fact that Eq. (3) is derived expressly for these concentration units. The data were fitted by a fourth-order polynomial for purposes of extrapolation to 0% and 100% of the phases present, and the intersections were taken as the equilibrium compositions. The use of a high-order polynomial obviated the need to impose any assumptions on the behavior of the intensity ratios with composition, and illustrates the nonlinear nature of Eq. (3).

At 800°C and below, the two-phase region consists only of sphalerite and thiogallate, and, as already noted, the parametric method is more accurate in this temperature range. Examples of its use are shown in Fig. 3. For the  $\text{ZnS}$ -rich end, the lattice constant of sphalerite,  $a$ , is plotted vs mol%  $\text{Ga}_2\text{S}_3$  using the angular position of the {331} sphalerite peak to calculate  $a$ . The solvus compositions at 700° and 750°C are located at 5.1 and 6 mol%  $\text{Ga}_2\text{S}_3$ . At the  $\text{ZnGa}_2\text{S}_4$ -rich end, the positions of the {400}, {316}, and {413} peaks were used to calculate  $a_t$  as a function of the mol%  $\text{Ga}_2\text{S}_3$ . The boundary between the one- and two-phase regions is 44%  $\text{Ga}_2\text{S}_3$  at 700°C and 41% at 800°C.

The  $\text{ZnS}$ - $\text{Ga}_2\text{S}_3$  phase diagram thus obtained from a combination of the two methods is shown in Fig. 4. Extrapolation of the phase boundaries between the one- and two-phase fields was used to determine the eutectoid composition and temperature, which were assumed to be the point of intersection of the high-temperature data. Since the data at high temperatures were limited, the extrapolation produces results which are accurate only to within about 1 mol%. Neverthe-

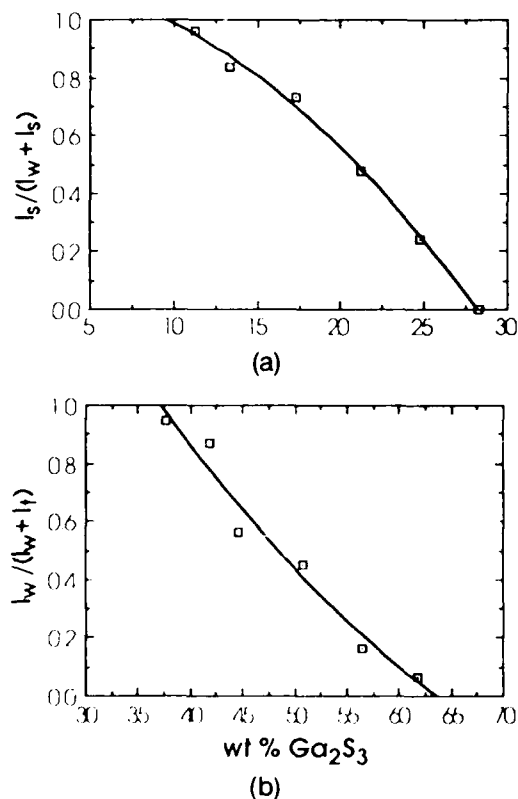


Fig. 2. Illustrating the use of the disappearing-phase method to determine the boundaries between (a) wurtzite and sphalerite at 850°C and (b) wurtzite and thiogallate at 900°C.

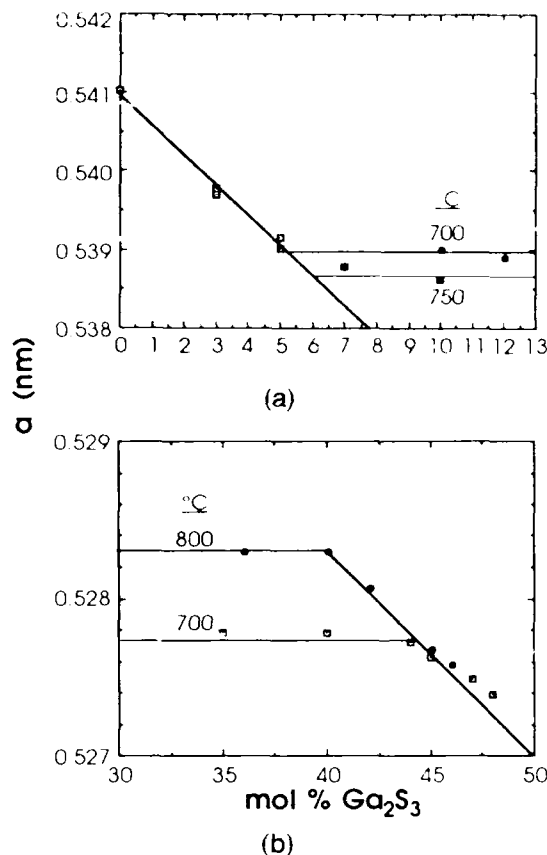


Fig. 3. Illustrating the use of the parametric method to determine (a) the S/(S + T) solvus at 700° and 750°C and (b) the T/(S + T) solvus at 700° and 800°C. In (b),  $a$  refers to  $a_t$ .

less, the coordinates of the intersection point, namely, 16%  $\text{Ga}_2\text{S}_3$  and 818°C, represent the best estimate of the eutectoid composition and temperature currently available. A similar extrapolation applied to the phase boundaries at the sphalerite-rich and thiogallate-rich ends of the phase diagram places the compositions of the reactant phases at ~9 and ~40 mol%  $\text{Ga}_2\text{S}_3$ , respectively. The phase boundaries indicated by the shaded curves in Fig. 1 are consistent with those determined quantitatively. It is difficult to determine how the errors in all the measurements propagate to the compositions and temperatures cited. We estimate that the eutectoid temperature is accurate to  $\pm 5^\circ\text{C}$  and the compositions accurate to  $\pm 1$  mol%  $\text{Ga}_2\text{S}_3$ .

On comparing our phase diagram with that of Malevskii,<sup>4</sup> we note that the accuracy of his diagram is limited by the much shorter reaction times used (400 h at 650°C; cf. more

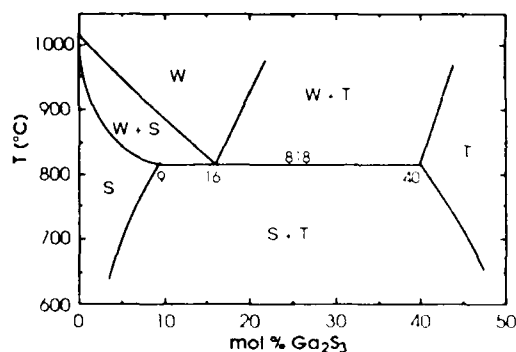


Fig. 4.  $\text{ZnS}$ - $\text{Ga}_2\text{S}_3$  phase diagram to 50 mol%, from 700° to 900°C.



than 1600 h at 700°C in our case), and the much larger intervals in composition employed, especially near the eutectoid composition (roughly 7 mol%). These two factors are undoubtedly responsible for the discrepancies between the two phase diagrams.

We note that the solubility of ZnS increases with increasing temperature. Consequently, both eutectoid decomposition and precipitation hardening can be potentially utilized to manipulate the mechanical properties of ZnS-Ga<sub>2</sub>S<sub>3</sub> ceramics, as discussed by Zhang *et al.*<sup>2</sup>

#### IV. Summary

The ZnS-Ga<sub>2</sub>S<sub>3</sub> phase diagram, from 700° to 900°C and to 50 mol% Ga<sub>2</sub>S<sub>3</sub>, was determined using X-ray diffraction techniques from samples prepared via the solid-state reaction of powders. The wurtzite (W), sphalerite (S), and tetragonal thiogallate (T) phases all exist over a considerable range of stoichiometry. There is a eutectoid reaction at  $818 \pm 5^\circ\text{C}$  in which W ( $16 \pm 1$  mol%) decomposes to S ( $9 \pm 1\%$ ) + T ( $40 \pm 1\%$ ). The solubility of Ga<sub>2</sub>S<sub>3</sub> in ZnS increases with increasing temperature below the eutectoid temperature.

#### References

- <sup>1</sup>W.W. Chen, J.M. Zhang, A. J. Ardell, and B. Dunn, "Solid-State Phase Equilibria in the ZnS-CdS System," *Mater. Res. Bull.*, **23**, 1667-73 (1988).
- <sup>2</sup>J.M. Zhang, W.W. Chen, B. Dunn, and A. J. Ardell, "Phase Diagram Studies of ZnS Systems", pp. 35-40 in Proceedings of the Society of Photo-Optical Instrumentation Engineers, Vol. 968, *Ceramics and Inorganic Crystals for Optics, Electro-Optics, and Nonlinear Conversion*, Edited by R.W. Schwartz, Society for Photo-Instrumentation Engineers, Bellingham, WA, 1988.
- <sup>3</sup>A. S. Gates and J. G. Edwards, "Vapor Pressures, Vapor Compositions, and Thermodynamics of the ZnGa<sub>2</sub>S<sub>4</sub>-ZnGa<sub>4</sub>S<sub>6</sub> System by the Simultaneous Knudsen and Dynamic Torsion-Effusion Method," *J. Phys. Chem.*, **82**, 2789-97 (1978).
- <sup>4</sup>A. Yu. Malevskii, "Ranges of Isomorphic Replacement in the System ZnS-Ga<sub>2</sub>S<sub>3</sub>," *Eksp. Issled. Obl. Geokhim. Kristallogr. Redk. Elem., Akad. Nauk SSSR, Inst. Mineral., Geokhim. Kristallogr. Redk. Elem.*, **12**, 20 (1967).
- <sup>5</sup>P. Wu, X.-C. He, K. Dwight, and A. Wold, "Growth and Characterization of Zinc and Cadmium Thiogallate," *Mater. Res. Bull.*, **23**, 1605-609 (1988).
- <sup>6</sup>G. B. Carpenter, P. Wu, Y.-M. Gao, and A. Wold, "Redetermination of Crystal Structure of Zinc Thiogallate," *Mater. Res. Bull.*, **24**, 1077-82 (1989).
- <sup>7</sup>D. L. Chess, C. A. Chess, and W. B. White, "Physical Properties of Ternary Sulfide Ceramics," *Mater. Res. Bull.*, **19**, 1551-58 (1984).
- <sup>8</sup>B. D. Cullity, *Elements of X-ray Diffraction*, 2d ed., p. 369, Addison-Wesley, Reading, MA, 1978.
- <sup>9</sup>H. P. Klug and L. E. Alexander, *X-ray Diffraction Procedures*, p. 410, Wiley, New York, 1954.
- <sup>10</sup>W. Dollase; unpublished research. □

## SOLID-STATE PHASE EQUILIBRIA IN THE ZnS-CdS SYSTEM

W. W. Chen, J. M. Zhang, A. J. Ardell, and B. Dunn  
Department of Materials Science and Engineering  
University of California  
Los Angeles, California 90024

(Received August 19, 1988; Communicated by A. Wold)

### ABSTRACT:

The ZnS-rich region of the ZnS-CdS phase diagram, up to 18 mol % CdS, was studied over the temperature range 700 to 950 °C, and the boundaries describing the equilibria between the sphalerite and wurtzite solid solutions were determined. X-ray diffraction analysis was the principal technique used, the phase boundaries being determined by the lattice-parametric and disappearing phase methods. The results indicate that the solubility of CdS in ZnS is extensive in both the sphalerite and wurtzite phases, with CdS stabilizing the wurtzite phase.

MATERIALS INDEX: zinc, sulfides, cadmium

### Introduction

The II-VI compound ZnS is technologically important due to its infrared transmitting and luminescent properties. Although many of its optical properties are adequate for various applications, there is considerable interest in improving its mechanical behavior. One method for hardening and toughening ceramic materials is by the incorporation or precipitation of a second phase in the matrix. This can be accomplished by a variety of methods, including thermal or thermo-mechanical processing to control solid-state reactions, which is the route we are pursuing. To utilize this approach a knowledge of the phase diagrams of the systems of potential interest is necessary.

ZnS is known to exist in two polymorphic modifications, sphalerite (cubic, zinc-blende) and wurtzite (hexagonal). The cubic form is stable at low temperatures and transforms to wurtzite at 1020 °C (1). The sphalerite-wurtzite (S-W) transition is affected by the addition of solutes, but knowledge of the phase equilibria is sparse. We selected the ZnS-CdS system for study because the optical properties of CdS are such that ZnS-CdS solid solutions or two-phase mixtures are likely to retain the excellent infrared transmission characteristics of pure ZnS.

CdS forms a complete series of solid solutions with wurtzite at high temperatures ( $T > 975$  °C) (2), but the only work on the phase equilibria at lower temperatures is a study conducted under hydrothermal conditions over the temperature range 250-450 °C (3). Those conditions and temperatures, however, are not practical for the thermal processing treatments we believe are required to produce strengthening and toughening. In this investigation, the phase boundaries between the ZnS-rich sphalerite and wurtzite solid solutions were determined over the temperature range 700-950 °C.

### Experimental

Samples were prepared from weighed amounts of cubic ZnS (99.9 %, Aesar) and hexagonal CdS (99.9 + %, Aesar) powder and mixed. The typical sample weighed at least 1 g, and alloys containing up to 18 mol % CdS were investigated. Approximately 0.2 g of each mixture was transferred to a silica ampoule, evacuated to  $2 \times 10^{-2}$  torr, and heated to 120 °C for 10 to 15 minutes to remove adsorbed water. The ampoule was then sealed and isothermally annealed at the desired temperature for times ranging from 1 to 4 weeks. X-ray diffraction analysis using monochromatic Ni-filtered  $\text{CuK}\alpha$  radiation was employed to identify the phases present and to determine their lattice constants. The phase boundaries were evaluated by using either the disappearing phase method or the parametric method (4). The X-ray intensities were recorded digitally in a step-scanning mode at intervals of  $0.01^\circ$  for 1 s or  $0.02^\circ$  for 10 s. Either NaCl or KCl powders were used as a standard, depending upon the amount of peak overlap with the samples, to obviate the need for precise alignment of the diffractometer.

### Results and Discussion

The phases detected by analysis of the peaks in the X-ray diffraction patterns in a large number of samples heat-treated at the four temperatures used in this study are presented in Fig. 1. This is a map describing the phase equilibria, in which the compositions of the phase boundaries are only approximately determined. The compositions were then determined more precisely using the X-ray methods mentioned above.

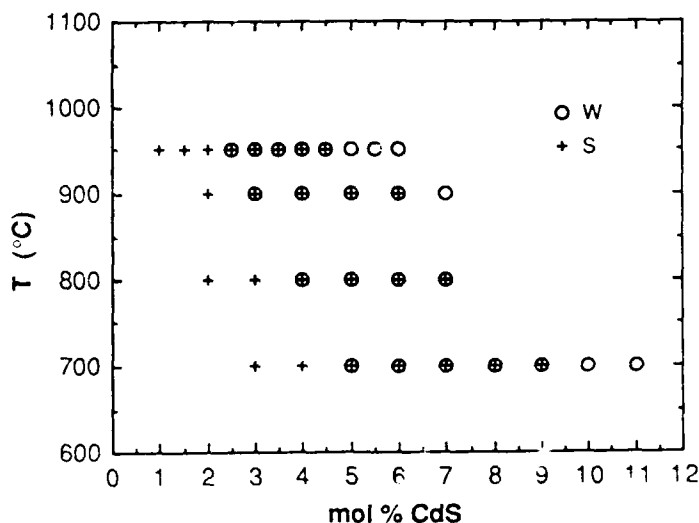


FIG. 1  
Identification of the phases observed on heating mixtures of  
ZnS and CdS powders for various times at the temperatures indicated.

An example of the determination of a phase boundary using the parametric method is shown in Fig. 2. In a single-phase region the lattice constant of the solid solution will vary with the concentration of solute if the atomic or ionic radii of the solvent and solute differ. Generally, this change is approximately linear and should be independent of the thermal history of the sample so long as equilibrium is reached. The solid line in Fig. 2 represents the variation of the lattice constant with composition of the sphalerite solid solution in the single-phase region. At the higher

reaction temperatures (900 and 950 °C) equilibrium was established relatively rapidly. The lattice constant of sphalerite is, of course, invariant in the two-phase  $S + W$  field, but the data are limited by the fact that the phase field is narrow. Hence, the number of data points at these two temperatures is small. As is evident in Fig. 2, the lattice constants for the two-phase mixtures in samples reacted at the lower temperatures (700 and 800 °C) continued to increase with increasing concentration of CdS, but not as rapidly as in the single-phase solid solution. This is probably due to the incomplete establishment of equilibrium. Consequently, the accuracy of the sphalerite solvus determined from the parametric method is not as valid as those at 900 and 950 °C due to the variance of the lattice constant values in the two-phase region. For this reason we relied on the disappearing phase method to determine the phase boundaries at the lower temperatures.

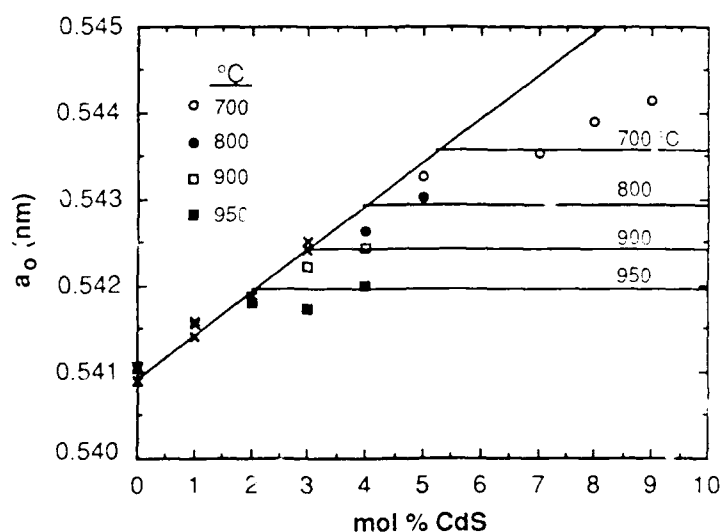


FIG. 2

The variation of the lattice constant of sphalerite,  $a_0$ , as a function of the CdS content of the mixtures prepared. The points indicated by  $\times$  apply to the single phase solid solution of CdS in ZnS.

The parametric method was also used to determine the  $(S + W)/W$  phase boundary compositions at 900 and 950 °C. The  $c$  and  $a$  lattice constants both vary linearly with the CdS concentration in the single-phase wurtzite region, and the intersection between the horizontal and sloped lines is the solvus as shown in Fig. 3. The compositions of the wurtzite phase boundaries determined from both  $c$  and  $a$  parameters are consistent (~4 mol % CdS at 950 °C and 5.5 to 6 mol % CdS at 900 °C). The small number of data points determining the horizontal lines is due to the narrow compositional range of the two-phase field at these temperatures.

The disappearing phase method proved to be more reliable for determining the phase boundaries at the lower temperatures. The method is based upon the variation of the relative amounts of  $S$  and  $W$  along a tie-line in the two-phase field as the overall composition is changed (4). For example, the weight fraction of  $W$  should decrease to 0 as the composition approaches the  $S$  solvus, and since the intensity of a particular wurtzite peak,  $I_w$ , is proportional to the weight %  $W$  in the two-phase mixture, the ratio  $I_w/I_s$  should also approach a value of zero as the sphalerite solvus is reached ( $I_s$  is the intensity of a sphalerite peak). The solvus composition is determined from an extrapolation of the variation of  $I_w/I_s$  vs. weight % CdS to the zero ordinate value.

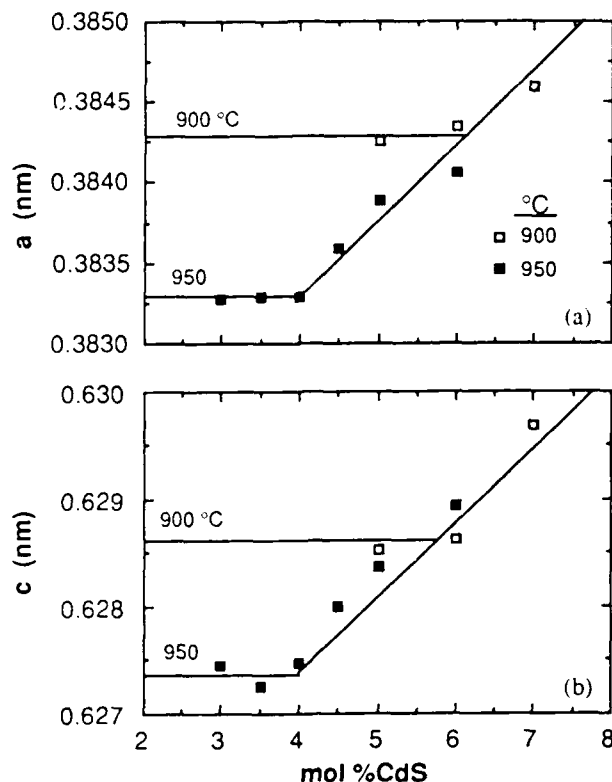


FIG. 3

Results obtained applying the parametric method; (a) illustrates the variation of the lattice constant *a*, while (b) illustrates the variation of the lattice constant *c* with the concentration of CdS.

The integrated intensities of the (311) sphalerite and the (21 $\bar{3}$ 1) wurtzite peaks were chosen for this analysis.  $I_s$  and  $I_w$  were computed using a numerical analysis program, subtracting the contribution of  $\text{CuK}\alpha_2$  radiation. Depending on the system being investigated, the relative ratio of the intensities can vary linearly or non-linearly with composition (4). From a cursory examination of the data, we decided to try a linear relationship and compare the results with the data in Fig. 1. The data are shown in Fig. 4, where it is evident that the assumed linear behavior is better obeyed by the data in Fig. 4a than in Fig. 4b.

From a combination of the two analytical methods used, the partial phase diagram for the ZnS-CdS system over the temperature range of this study is shown in Fig. 5a. The solid curves drawn in Fig. 5a are shown in Fig. 5b, where they are superimposed on the data from Fig. 1; the agreement is very good. We are therefore confident that the results obtained using the disappearing phase method are accurate, despite the scatter in Fig. 4b. The disappearing phase method succeeded where the parametric method failed because the integrated intensities of the broad peaks in the two-phase mixtures are more accurately measured than the positions of the peak maxima.

The partial ZnS-CdS phase diagram determined over the temperature range 250 to 450 °C under hydrothermal conditions by Kaneko *et al.* (3) exhibits features similar to those in Fig. 5, especially insofar as the solubility of CdS in ZnS decreases with increasing temperature. Kaneko *et al.* made no attempt to determine the phase boundaries, but it is evident that their two-phase equilibria are shifted to higher mol % CdS, and the compositional range of their two-phase field is much greater. The two phase diagrams can be reconciled only if the sphalerite phase is stabilized

under hydrothermal conditions, but there is no convincing evidence to suggest that this stabilization process occurs. Cherin et al. (5) found a two-phase mixture of sphalerite and wurtzite in their ZnS single crystals containing 5 mol % CdS. The crystals were grown in a temperature gradient of 925 to 950 °C using the iodine vapor transport method. Their result is entirely consistent with our phase diagram.

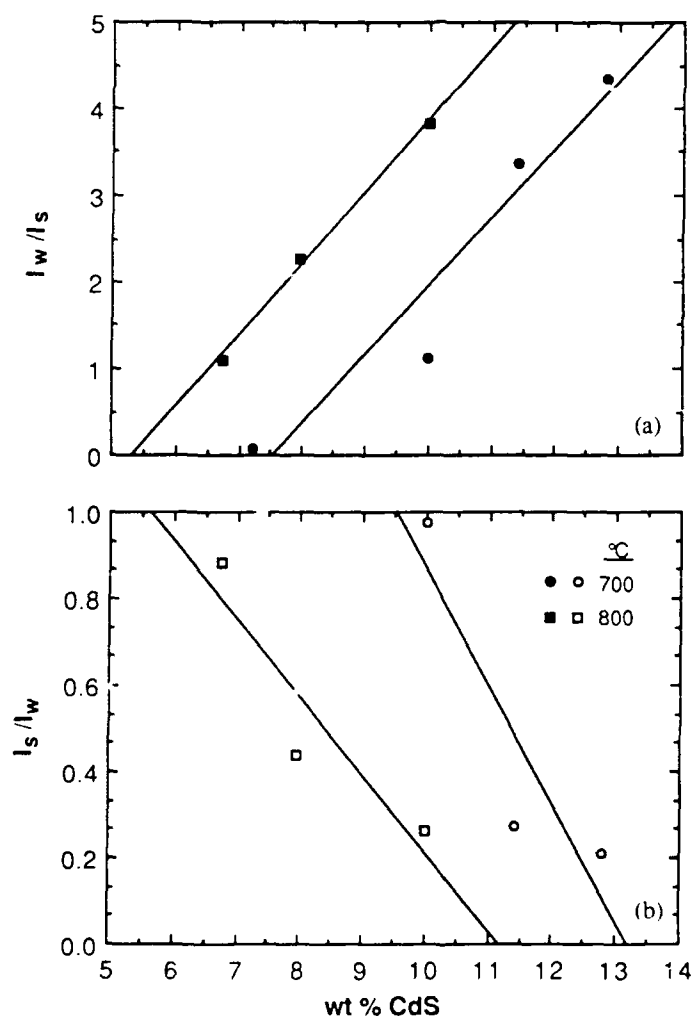


FIG. 4

Results obtained using the disappearing phase method: (a) The ratio of the intensities of the wurtzite {2131} peak and the sphalerite {311} peak,  $I_w/I_s$ , as a function of the concentration of CdS in weight %. In (b) the ratio of the intensities is inverted.

The use of differential thermal analysis for determination of the phase boundaries was attempted in several trial runs using pure ZnS. Since the enthalpy of the sphalerite to wurtzite transformation is 3.19 kcal/mol (6) in pure ZnS, the transition was not detected on heating and cooling

through 1020 °C. Thus, the small heat evolution during the transformation rendered thermal analysis ineffective for determining the phase diagram in this system.

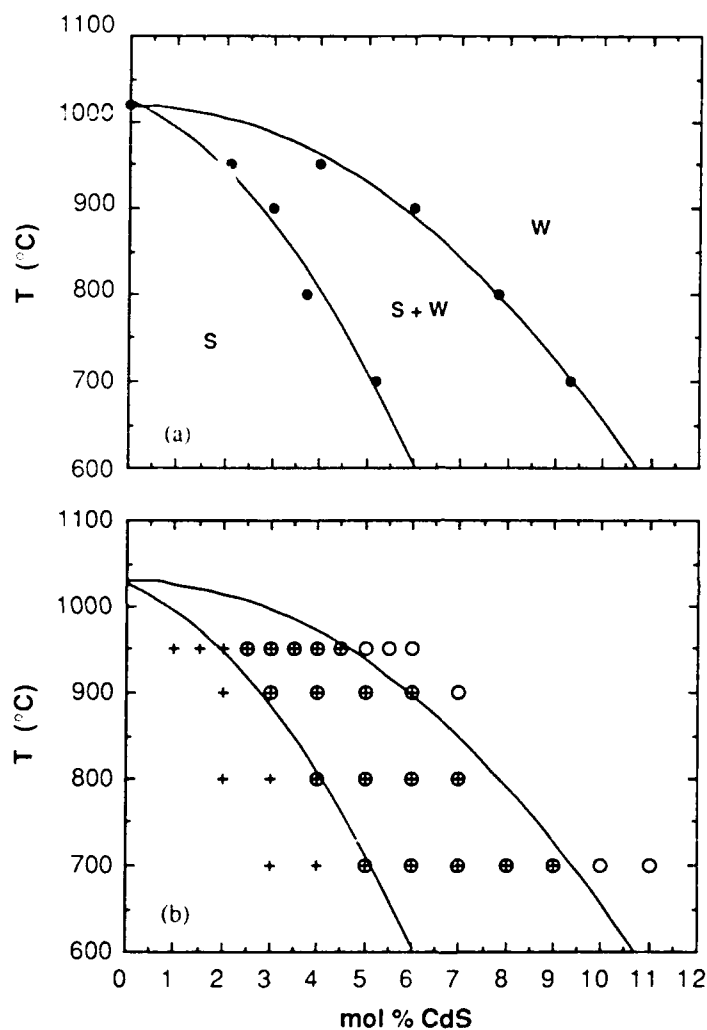


FIG. 5

(a) Partial phase diagram for the ZnS-CdS system over the temperature range 700 to 1100 °C. A comparison with the phases observed over the range of conditions in Fig. 1 is shown in (b).

#### Summary

The partial phase diagram for the ZnS-CdS system was determined over the temperature range 700 to 950 °C. Cubic and hexagonal solid solutions of ZnS were formed, and the boundaries of the two phase region were determined by the use of the parametric and disappearing phase methods.

### Acknowledgement

The authors are grateful to the Office of Naval Research, Contract No. N00014-87-K-0531, for sponsoring of this research. We also thank Professor W. A. Dollase for providing a copy of the computer program POW, used for calculating the integrated intensities employed in the disappearing phase method.

### References

1. A. T. Allen and J. L. Crenshaw, *Z. Anorg. Chem.*, **79**, 130 (1913).
2. F. A. Kröger, *Z. Krist.*, **A102**, 132 (1939).
3. S. Kaneko, H. Aoki, Y. Kawahara and F. Imoto, *J. Electrochem. Soc.*, **131**, 1445 (1984).
4. B. D. Cullity, **Elements of X-Ray Diffraction**, second edition, p. 369. Addison-Wesley, Reading, MA (1978).
5. P. Cherin, E. L. Lind and E. A. Davis, *J. Electrochem. Soc.*, **117**, 233 (1970).
6. G. Kullerud, *Norsk. Geol. Tidsskr.*, **32**, 61 (1953).



# PROCEEDINGS REPRINT

 SPIE—The International Society for Optical Engineering

*Reprinted from*

## Window and Dome Technologies and Materials II

**Paul Klocek**  
*Chair/Editor*

11-13 July 1990  
San Diego, California



**Volume 1326**

# Solid Solution Strengthening of ZnS

Jimin Zhang, W. W. Chen and A. J. Ardell

Department of Materials Science and Engineering  
University of California, Los Angeles, CA 90024, U. S. A.

## ABSTRACT

A series of ZnS-rich wurtzite solid solutions containing 8, 12 and 16 mol%  $\text{Ga}_2\text{S}_3$  has been prepared. The influences of the fabrication conditions and microstructure on the mechanical properties were examined. It has been demonstrated that  $\text{Zn}_{1-x}\text{Ga}_x\text{S}_{1+2x}$  is tougher and harder than pure ZnS due to a solid-solution strengthening effect. The hardness of the solid solutions increases with increasing concentration of  $\text{Ga}_2\text{S}_3$  and decreasing grain size, the grain-size dependence being of the Hall-Petch type. Finer-grained solid solutions with moderate concentrations of  $\text{Ga}_2\text{S}_3$  have the highest fracture toughness. Whereas the hardness increases monotonically with increasing mole fraction of  $\text{Ga}_2\text{S}_3$ , the fracture toughness is a maximum at around 12 %  $\text{Ga}_2\text{S}_3$ .

## 1. INTRODUCTION

ZnS is used as an infrared window material for applications in the 8-12  $\mu\text{m}$  range because of its adequate optical transmission and mechanical behavior. However, improvements in its fracture toughness, thermal shock resistance as well as erosion resistance are highly desirable for missile dome applications. To obtain useful optical properties and improved mechanical behavior requires a microstructure which is inhomogeneous with regard to deformation and fracture, but homogeneous for the wavelength of interest. Since multiphase materials are inherently undesirable for optical transmission, attempts were made to produce single-phase solid solutions of ZnS (or the solid solution plus very fine precipitates) which are not only infrared transmitting in the 8 to 12  $\mu\text{m}$  range but also possess improved mechanical properties. Solid-solution strengthening has been found in some ceramic systems<sup>1,2</sup>. In this study, ZnS- $\text{Ga}_2\text{S}_3$  solid solutions were synthesized to increase the mechanical strength of ZnS.  $\text{Ga}_2\text{S}_3$  was chosen as a second phase component for reasons discussed by Zhang et al<sup>3</sup>.

## 2. EXPERIMENTAL

ZnS-x mol%  $\text{Ga}_2\text{S}_3$  solid solutions (where x is 8, 12 and 16 respectively) were synthesized by sintering a physical mixture of powders of ZnS (99.99%, Aldrich) and  $\text{Ga}_2\text{S}_3$  (99.99%, Alfa). The solid-state reaction was completed after 18 hours at 925°C in  $\text{H}_2\text{S}$  atmosphere. The powders were identified as single-phase wurtzite (hexagonal, B4 structure) by X-ray diffraction analyses. A vibromill (8000 Mixer/Mill, SPEX) was used to reduce the size of the starting solid solution powders to about 3  $\mu\text{m}$ . The powder was cold-pressed in vacuum at 207 MPa and was subsequently hot-pressed in a molybdenum die. Table I lists the hot-pressing conditions ( $T_p$ , t and p are the hot-pressing temperature, holding time and pressure respectively) for all alloys and pure ZnS and Fig. 1 shows a schematic hot pressing schedule. The sample was heated at 300°C for 10 minutes to eliminate water adsorbed on the powders, then continuously heated at a constant rate of 20°C/min to 900°C, after which the pressure (138 MPa) was applied. Temperature and pressure were held for about 20 to 40 minutes and then usually the pressure was released and sample slowly cooled to room temperature. The densities of the hot-pressed pellets were measured using a liquid immersion technique based on the ASTM standard<sup>4</sup>.

A series of hot-pressed pellets was sealed into quartz ampoules and solid-solution treated in the wurtzite phase field for various lengths of time. The heat-treatment temperatures were selected according to the partial ZnS- $\text{Ga}_2\text{S}_3$  phase diagram we established earlier<sup>3</sup>. The purpose of the treatments is twofold: (a) to ensure that the specimen is completely transformed to wurtzite; (b) to grow grains of different sizes. Pure ZnS was annealed at 1080°C and all three solid solutions at 940°C. The ampoules were water-quenched to room temperature immediately after all reaction treatments. Microprobe analysis and EDS were performed on ZnS and all the solid solutions, and the results confirmed the expected compositions.

The hardness and fracture toughness were evaluated using the Vickers indentation technique. The hardness,  $H$ , in GPa, is obtained using the formula

$$H = 18.169 \frac{P}{a^2} \quad (1)$$

where  $P$  is the applied load in grams and  $a$  is the diagonal length of the Vickers indentation in  $\mu\text{m}$ .

Table 1. Hot Pressing Parameters.

Materials	$T_p$ °C	$t$ min	$p$ MPa	Density Mg/m <sup>3</sup>	% Density
ZnS	850	20-40	134	4.042	99.01
ZnS-8% Ga <sub>2</sub> S <sub>3</sub>	900	35	124	4.001	99.60
ZnS-12% Ga <sub>2</sub> S <sub>3</sub>	900	40	124	3.965	99.61
ZnS-16% Ga <sub>2</sub> S <sub>3</sub>	900	20	103	3.907	99.10

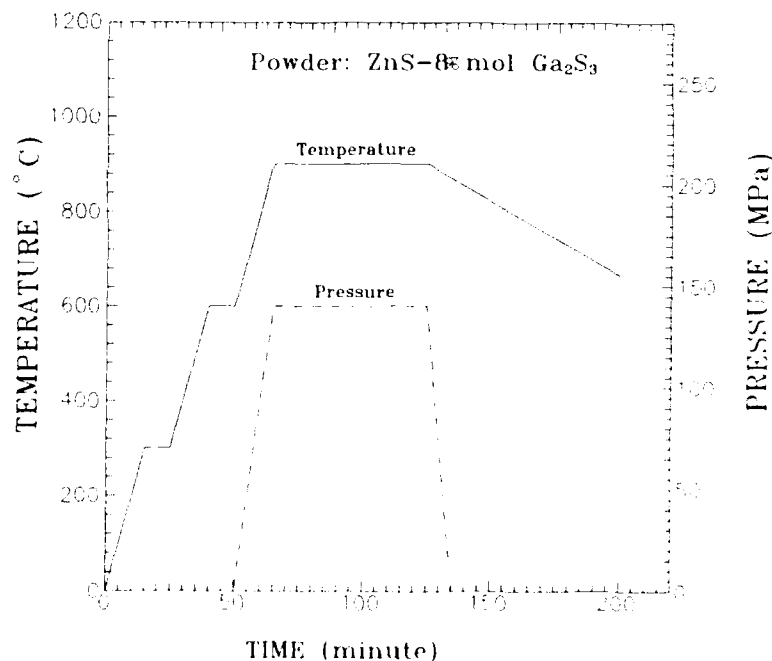


Fig. 1. Hot pressing program

Fracture toughness measurement by the Vickers indentation technique is based on indentation fracture mechanics<sup>5</sup>. Because of its uniquely simple and economic nature, this technique has been widely used for measuring fracture toughness, especially for small specimens. The fracture-toughness data obtained by the indentation

technique are accurate to within either 10% if Young's modulus is known or 30% if Young's modulus is not known<sup>6</sup>. The fracture toughness for a median/radial crack system,  $K_{Ic}$ , can be expressed as<sup>7</sup>

$$K_{Ic} = \delta \left( \frac{E}{H} \right)^{1/2} \frac{P}{C^{3/2}} \quad (2)$$

where  $\delta$  is a material-independent constant ( $\sim 0.016$ ),  $E$  is Young's modulus and  $C$  is the crack length.

Specimens approximately one quarter of the 12.4 x 2 mm discs were first cold-mounted in epoxy and then ground and polished. Final polishing was done on a standard metallographic wheel using 0.05  $\mu\text{m}$  alumina polishing powder. Considerable care was taken to ensure smooth and residual-stress free surfaces to measure hardness and toughness. A Microhardness Tester (MicroMet II, Buehler) was used to measure  $H$  for at least three different loads (typically 200, 500 and 1000 g) and more than 18 indentations for each specimen were taken using a loading time of 15 s. The indentation impression size and Vickers indentation crack length were measured immediately after unloading. It was observed that cracks propagate in an intragranular mode for all the specimens. Young's modulus,  $E$ , for all the specimens was measured using a Nanoindenter, yielding an average value of 90 GPa. This value was used in the calculations of  $K_{Ic}$  according to equation (2).

### 3. RESULTS AND DISCUSSION

Since the highest pressure is limited by the strength of the die material, it was necessary to explore different conditions of  $T_p$ ,  $p$  and  $t$  for hot pressing. The optimum hot-pressing condition for the ZnS-Ga<sub>2</sub>S<sub>3</sub> solid solutions is  $T_p = 900^\circ\text{C}$ ,  $p = 124$  to 138 MPa and  $t = 20$  to 40 minutes. The conditions used to produce specimens exceeding 99.0% of their theoretical densities are listed in Table 1.

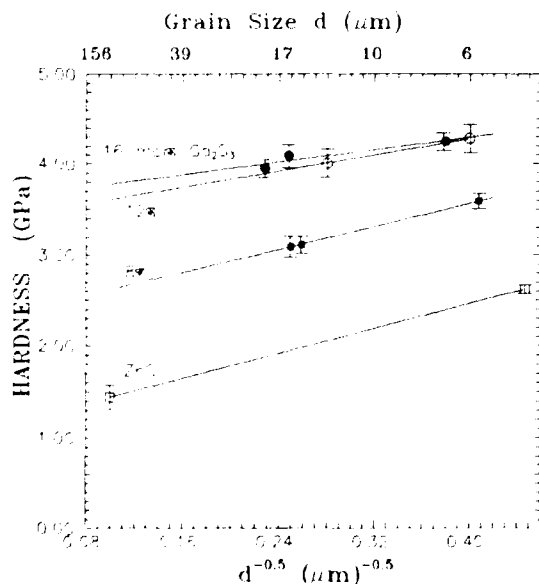


Fig. 2. Hardness vs. the reciprocal square root of the grain size for ZnS and the solid solutions

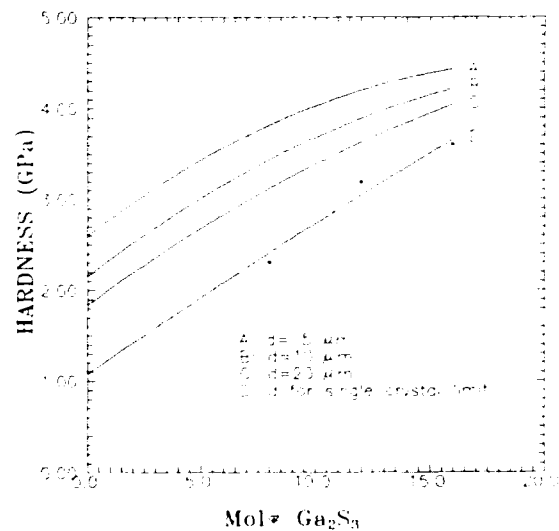


Fig. 3. Hardness vs. concentration of Ga<sub>2</sub>S<sub>3</sub>. The curve A, B and C were obtained from the curves fitted to the data in Fig. 2.

The hardness values of the specimens as a function of grain size,  $d$ , are listed in Table 2, and plotted as a function of  $d^{-1/2}$  in Fig. 2. It can be seen that hardness increases as  $d$  decreases for all three solid solutions and pure ZnS. This indicates that smaller grains produce higher resistance to dislocation motion, possibly due to

dislocation pile-ups at grain boundaries. Since the hardness of a ceramic material is about three times its yield stress<sup>8</sup>, the dependence of  $H$  on  $d$  can be expressed using the Hall-Petch equation:

$$H = H_0 + kd^{-1/2} \quad (3)$$

where  $H_0$  and  $k$  are constants. The present experimental data are in good agreement with equation (3).

Table 2. Hardness and toughness of pure ZnS and the ZnS-Ga<sub>2</sub>S<sub>3</sub> alloys as a function of grain size.

Materials	Grain Diameter (μm)	Hardness (GPa)	Toughness (MN/m <sup>3/2</sup> )
ZnS	5	2.62 ± 0.09	0.50 ± 0.10
	100	1.44 ± 0.23	0.40 ± 0.09
ZnS-8% Ga <sub>2</sub> S <sub>3</sub>	6	3.59 ± 0.14	0.72 ± 0.09
	16	3.11 ± 0.16	0.68 ± 0.10
	18	3.09 ± 0.20	0.66 ± 0.15
ZnS-12% Ga <sub>2</sub> S <sub>3</sub>	6	4.27 ± 0.27	0.77 ± 0.15
	14	4.01 ± 0.27	0.70 ± 0.12
ZnS-16% Ga <sub>2</sub> S <sub>3</sub>	7	4.25 ± 0.17	0.62 ± 0.09
	16	4.09 ± 0.22	0.54 ± 0.10
	20	3.95 ± 0.17	0.53 ± 0.09

The hardness as a function of the amount of Ga<sub>2</sub>S<sub>3</sub> in solid solution is plotted in Fig. 3. The data were extracted from Fig. 2, with curve D obtained by extrapolating to  $H = H_0$  at  $d^{-1/2} = 0$ . It is clear from Fig. 3 that the hardness of the solid solutions increases monotonically with Ga<sub>2</sub>S<sub>3</sub> content. The alloy with 16 % Ga<sub>2</sub>S<sub>3</sub> was about twice as hard as pure ZnS in the grain size range studied. The increase in the hardness for the solid solutions results from the interactions between dislocations and defects induced by the Ga<sub>2</sub>S<sub>3</sub> dissolved in the crystals.

The resistance to dislocation motion that constitutes solid-solution strengthening can come from one or more of the following factors. First, a stress field will be induced by the relative size difference between Ga and Zn ions; the actual difference is about 25%, the sizes of Zn and Ga ions being 0.083 and 0.062 nm respectively. In addition, the substitution of two Ga<sup>3+</sup> ions for three Zn<sup>2+</sup> will create a vacancy to preserve electrical neutrality, and the hardening can be increased by an associated vacancy-Ga<sup>3+</sup> defect. Additionally, a difference in the effective shear modulus between Ga and Zn could be an important factor, and an electrical interaction between dislocations and Ga<sup>3+</sup> ions or vacancy-Ga<sup>3+</sup> complex could impede dislocation movement. Finally, the spatial distribution of the solute ions might not be completely random, and either short-range ordering or clustering would produce a hardening effect. Many of these mechanisms are known to be effective in inhibiting the motion of dislocations in metallic alloys and can be expected to operate in ceramic alloys as well. Identifying the specific mechanism(s) requires additional research, however.

Fracture toughness for all the specimens is plotted versus  $d^{-1/2}$  in Fig. 4. It is readily seen that all the solid solutions are tougher than ZnS, with ZnS-12 % Ga<sub>2</sub>S<sub>3</sub> having the highest toughness values. Figure 4 also shows that  $K_{Ic}$  is approximately proportional to  $d^{-1/2}$  for both pure ZnS and the solid solutions in the grain size range covered. The cracks emanating from the microhardness indentations are shown in Fig. 5, where it is evident that the crack patterns in the solid solutions are more irregular than those of pure ZnS, the cracks often curving, branching and deviating from the plane intersecting the corners of the indentation. The micrographs in Fig. 5 indicate that propagating cracks are more easily deflected in the solid solutions than in pure ZnS.

Of all toughening mechanisms discussed by Swain<sup>9</sup>, transformation toughening is unlikely to be of any importance to this system because there is only a 0.2% volume change accompanying the transformation from wurtzite (W) to sphalerite (S) (the cubic form of the ZnS solid solutions, which has a smaller molecular volume), though it is possible to induce the W-S transformation by an applied stress<sup>10</sup>. On the other hand, microcrack toughening is one of the most likely mechanisms to cause crack deflection in the ZnS solid solutions. Microcrack toughening has been found to be an effective toughening mechanism in many ceramic materials. In non-cubic ceramics produced by hot pressing, microcracks develop on cooling from the processing temperature. According to Rice et al.<sup>11</sup> microcrack toughening by this mechanism is grain-size dependent, the number of microcracks per unit volume increasing with increasing grain size while the elastic energy absorbed per microcrack decreases with increasing grain size. This model therefore predicts an optimum value of the grain size which maximizes  $K_{Ic}$ .

Lewis et al.<sup>12</sup> have shown that  $K_{Ic}$  for CVD-grown cubic ZnS behaves similarly in that  $K_{Ic}$  is maximized at some value of  $d$ . They suggest that the grain-size dependence of  $K_{Ic}$  is due to crack nucleation through dislocation pile-ups at grain boundaries, and the decrease in  $K_{Ic}$  for very small grain sizes is attributed to void formation in a spherical zone beneath the Vickers indentation contact area. Although this is not a microcrack toughening mechanism, the dependence of  $K_{Ic}$  on  $d$  can nevertheless be similar for cubic and non-cubic materials.

Whereas a maximum value of  $K_{Ic}$  as a function of  $d$  is not observed in Fig. 4, the mechanism of Rice et al.<sup>11</sup> could nevertheless be viable in hexagonal ZnS. When the non-cubic polycrystalline ZnS solid solutions are cooled from the hot-pressing temperature to room temperature, intercrystalline microstresses can be expected to develop as a result of the thermal-expansion anisotropy of the grains. The mechanism proposed by Lewis et al.<sup>12</sup> could also contribute to the increasing toughness, however, because there is no reason why plasticity (as opposed to microcrack) toughening cannot play a role in augmenting the toughness of non-cubic materials. At this stage of the research there is no way of evaluating the relative importance of the microcrack vs. plasticity toughening mechanisms.

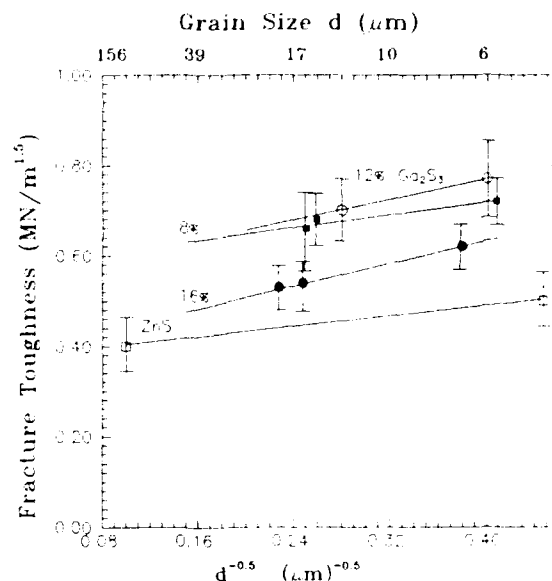


Fig. 4. Fracture toughness vs. the reciprocal square root of the grain size for ZnS and the solid solutions

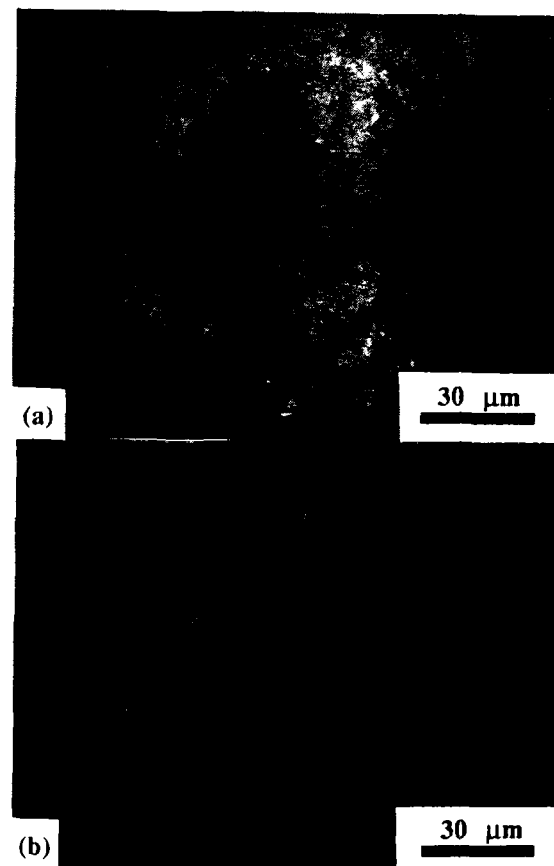


Fig. 5. Vickers hardness indentations under a load of 200 g for (a) pure ZnS and (b) for ZnS-16% Ga<sub>2</sub>S<sub>3</sub>

It can be observed in Fig. 4 that the effect of the  $\text{Ga}_2\text{S}_3$  concentration on the toughness of the solid solutions is not a monotonic function. Of the three ceramic alloys, ZnS-12%  $\text{Ga}_2\text{S}_3$  has the highest toughness values, implying that there is an optimum  $\text{Ga}_2\text{S}_3$  concentration for fracture toughness. The underlying physical reason for an optimal concentration of  $\text{Ga}_2\text{S}_3$  is currently not understood and remains another interesting topic for future research.

#### 4. SUMMARY

1. The incorporation of  $\text{Ga}_2\text{S}_3$  into ZnS improves both the hardness and toughness of ZnS.
2. The hardness of the ZnS- $\text{Ga}_2\text{S}_3$  solid solutions is proportional to the amount of  $\text{Ga}_2\text{S}_3$  in the solutions.
3. The hardness increases as the grain size decreases for all three solid solutions and pure ZnS. It is consistent with the Hall-Petch relation:  $H = H_0 + kd^{1/2}$ .
4. All the solid solutions are tougher than ZnS. A finer grain size results in higher toughness. However, the dependence of fracture toughness of the solutions on the solute content is not a monotonically increasing function. It seems that there is an optimum composition for the fracture toughness.

#### 5. ACKNOWLEDGEMENT

The authors are grateful to the Office of Naval Research, Contract No. N00014-87-K-0531, for their financial support of this work. The authors wish to thank Professor B. Dunn for his help during this entire investigation. The assistance of Drs. D. Kipp and T. Vanderah of the Naval Weapons Center, China Lake, CA, in the preparation of the solid-solution powders is greatly appreciated. Thanks are also due to Dr. D. B. Marshall of the Science Center of Rockwell International, Thousand Oaks, CA, for his help in the measurement of Young's modulus of the specimens.

#### 6. REFERENCES

1. N. S. Stoloff, D. K. Lezins and T. L. Johnson, "Effect of Temperature on the Deformation of KCl-KBr Alloys" *J. Appl. Phys.*, **34**, 3315-3322, (1963).
2. T. S. Liu, R. J. Stokes and C. H. Li, "Fabrication and Plastic Behavior of Single-Crystal MgO-NiO and MgO-MnO Solid Solution Alloys" *J. Am. Ceram. Soc.*, **47**, 276-279, (1964).
3. J. Zhang, W. W. Chen, A. J. Ardell and B. S. Dunn, "Solid State equilibria in the ZnS- $\text{Ga}_2\text{S}_3$  system" *J. Am. Ceram. Soc.* (to be published).
4. ASTM designation c-20-87, *1989 Book of ASTM Standards*, Vol.15.01; 5-7.
5. B. R. Lawn and D. B. Marshall, "Hardness, Toughness and Brittleness: Indentation Analysis," *J. Am. Ceram. Soc.*, **62**, 347-50, (1979).
6. A. G. Evans and E. A. Charles, "Fracture Toughness Determinations by Indentation", *J. Am. Ceram. Soc.*, **59**, 371-372, (1976).
7. G. A. Anstis, P. Chantikul, B. R. Lawn and D. B. Marshall, "A Critical Evaluation of Indentation Techniques for Measuring Fracture Toughness: I, Direct Crack Measurements," *J. Am. Ceram. Soc.*, **64**, 533-543, (1981).
8. S. S. Chiang, D. B. Marshall and A. G. Evans, "The Response of Solids to Elastic/Plastic Indentation. I. Stresses and Residual Stresses", *J. Appl. Phys.*, **53**, 298-311, (1982).
9. M. V. Swain, "Toughening Mechanisms for Ceramics", *Materials Forum*, **13**, 237-253, (1989).
10. G. Kullerud, "The FeS-ZnS System -- a Geological Thermometer", *Norsk Geologisk Tidsskrift*, **32**, 61-147, (1953).
11. R. W. Rice, S. W. Freiman and P. F. Becher, "Grain-Size Dependence of Fracture Energy in Ceramics: I, Experiment", *J. Am. Ceram. Soc.*, **64**, 345-354, (1981).
12. K. L. Lewis, A. M. Pitt, J. A. Savage, J. E. Field and D. Townsend, "The Mechanical Properties of CVD-Grown Zinc Sulfide and Their Dependence on the Conditions of Growth", *Proc. Ninth Int. Conf. on Chemical Vapor Deposition*, **84-6**, The Electrochemical Society Inc. Pennington, NJ, 530-545, (1984).

MEASUREMENT OF THE FRACTURE TOUGHNESS OF CVD-GROWN  
ZnS USING A MINIATURIZED DISK-BEND TEST

Jimin Zhang and Alan J. Ardell

November 1990

Department of Materials Science and Engineering

University of California

Los Angeles, CA 90024

Submitted to JOURNAL OF MATERIALS RESEARCH



## ABSTRACT

Novel apparatus and methodology have been developed for measuring the fracture toughness of ceramics using small disk-shaped samples 3 mm in diameter. The method involves the Vickers indentation of specimens ranging in thickness from 300 to 700  $\mu\text{m}$ , and testing them in a ring-on-ring bending mode. Experiments on CVD-grown ZnS have been used to evaluate the technique. The apparent fracture toughness of this material increases with increasing crack length (R-curve behavior). This behavior is analysed using established equations in conjunction with a new graphical method that obviates the need for measuring the apparent toughness of samples containing very large cracks. The fracture toughness at "infinite" crack length,  $0.87 \pm 0.08 \text{ MPa}\cdot\text{m}^{1/2}$ , is in excellent agreement with the values obtained by conventional methods. The effect of sample size on the accuracy of the results is thoroughly discussed. The thickness,  $t$ , of the sample should exceed by a factor of ten the initial crack length produced by the indentation. Also, since samples are tested at various indentation loads,  $P$ , the ratio of their thicknesses should be chosen to satisfy the condition  $t \propto P^{2/3}$ . The importance of several parameters in the design of the apparatus is also discussed.

## I. INTRODUCTION

Many techniques have been developed for measuring the fracture toughness of ceramic materials, the most common ones being the double torsion technique and the double cantilever beam test. These methods require the use of relatively large samples, and in this sense are material intensive. It often happens in materials research and development programs that the quantity of material available is limited, hence a method using small specimens to measure fracture toughness would be preferred. The indentation toughness method<sup>1</sup> has evolved as a particularly useful one because it is fast, simple and can provide useful data from quite small samples. Nevertheless, there are limitations associated with this method, which arise mainly from uncertainties in the measurement crack length, the development of the pattern of cracks and the presence of residual stresses at the surface. Also, the indentation toughness method cannot provide information on the increase in the resistance to crack propagation with increasing crack length (R-curve behavior).

Over the past ten years or so several different kinds of tests have been developed specifically to investigate the mechanical behavior of small specimens. The miniaturized disk-bend test (MDBT), is but one of several such tests, the history and variety of which have been recently reviewed by Lucas<sup>2</sup>. We have developed our own MDBT apparatus, as well as procedures for measuring the yield stress of metals and alloys<sup>3</sup>, and decided to explore the possibility of utilizing it additionally for measuring the fracture toughness of brittle solids. This decision was motivated by our recent attempts to develop stronger and tougher ZnS-based ceramics for infrared window applications<sup>4-6</sup>. We typically prepare small quantities of ceramic alloys, e. g. alloys in the ZnS-Ga<sub>2</sub>S<sub>3</sub> system, and use the indentation toughness method to compare the fracture toughness of these alloys as a function of composition and the processing conditions. The information so gathered is quite useful, but limited for the reasons already mentioned.

We therefore decided to explore the possibility of using the "controlled flaw" method to measure the fracture toughness,  $T_{\infty}$ , of several ceramic materials. The basic procedure in conventional testing is to first indent the specimen and then measure its fracture strength in a bend test, such as four-point bending or ring-on-ring bending. The latter employs circular specimens and has been used to measure the fracture toughness of flat disks of glass and alumina<sup>7</sup> and yttria<sup>8</sup>. The equations of fracture mechanics are then applied and  $T_{\infty}$  is extracted from analysis of the data.

In this paper we describe our adaptation of the controlled flaw technique using samples scaled down in size for testing in the MDBT apparatus<sup>3</sup>. The test is actually a miniaturized ring-on-ring disk-bend fracture toughness test (MDBFTT), with which  $T_{\infty}$  can be evaluated. The samples used in this test are disks 3 mm in diameter and ranging in thickness from 300 to 700  $\mu$ m. Fracture toughness can be obtained by this method without measuring the crack lengths, thereby eliminating the uncertainties associated with such measurements.

There are many advantages to the MDBFTT. First, it provides an efficient method for testing many specimens prepared from a limited supply of material, which as already noted is extremely valuable in a materials synthesis program in which small quantities of material are produced. Second, when the size of the ceramic specimens is so small, the indented crack is likely to be the predominant flaw, so that more reliable statistical results can be obtained. Third, sample preparation is easy, and no special equipment is needed beyond that required for making samples for transmission electron microscopy. Additionally, the ring-on-ring geometry in the miniaturized test described here has the same advantages of this geometry for larger samples, namely constant stress on the tensile surface, easy alignment, more accurate measurement of the stress, and a biaxial state of stress, which obviates the need for a special orientation of the crack (cf. four-point bending, in which the crack plane must be perpendicular to the tensile axis).

## II. EXPERIMENTAL

The MDBFTT apparatus is a minor variation of the test facility designed in our laboratory for bend-testing more ductile materials<sup>3</sup>; it is illustrated schematically in Fig. 1. The load is transmitted by a punch (0.981 mm in diameter) and a 1 mm diameter ball bearing through a stainless steel loading ring with an outer and inner diameters of 0.9 and 0.66 mm, respectively. In the original test rig the load is transmitted to the sample directly by the ball bearing, but in this adaptation it serves to assure the alignment of the loading ring along the vertical axis. The entire loading assembly is directed through the guide cylinder, which is bored to a diameter of 1.005 mm. The inner diameter of the lower die is 2 mm, hence the samples are supported over an annulus of 0.5 mm. Both the die and the cylinder are made of D2 tool steel. Shims of different thickness are placed between the upper and lower housings to accommodate specimens thicker than the 300  $\mu\text{m}$  recess in the lower die.

The material used for these initial tests was ZnS prepared by chemical vapor deposition (CVD) and obtained from Morton International. ZnS was chosen because it is commercially available, provides a reference material in our research on the development of ZnS-based infrared transmitting ceramics<sup>4-6</sup>, and has well-characterized physical and mechanical properties, including its fracture toughness as measured by conventional methods. Selected properties of this material are listed in Table 1.

The material was first cut into slices varying from 350 to 800  $\mu\text{m}$  in thickness, depending on the ultimate thickness desired for the disk specimens, using a low-speed diamond saw (South Bay Technology model 650). All the slices were cut along a plane which is perpendicular to the CVD growth plane, thus the normal direction of the disks is perpendicular to the CVD growth direction. There is no difference in the hardness parallel and perpendicular to the growth direction. Disks 3 mm in diameter were then trepanned from the slices using an ultrasonic disk cutter (Gatan, model

601) with SiC powder as an abrasive slurry. The disks were then metallographically polished through 0.05  $\mu\text{m}$  alumina powder. The specimens were examined under the optical microscope after final polishing to assure that the surfaces were scratch-free and that no other pre-existing flaws were present. The thicknesses of the specimens were chosen according to the magnitude of the indentation load; 300  $\mu\text{m}$  thick samples were used for the smallest load (0.98 N), whereas for the maximum load (19.6 N) it was necessary to use specimens 700  $\mu\text{m}$  thick. The thicknesses of the samples were measured to within  $\pm 2 \mu\text{m}$  using a micrometer.

Vickers indentations were made in the center of the disk using a Buehler Micromet microhardness tester for loads up to 1 kg, and a Tukon microhardness tester for larger loads. The same loading time was used over the entire range of loads, from 100 g to 2 kg (0.98 to 19.6 N). The centers of the disks were located to within  $\pm 10 \mu\text{m}$  before indentation using the micrometer stage built into the hardness tester. Unindented disks were also tested to measure their flexural strength. At least five specimens were tested for each indentation load. All the specimens were examined in the optical microscope after testing to check whether or not the Vickers indentations served as the origins of the failures. Results from samples that did not meet this criterion were discarded (roughly 20 % of the tests run at the smallest indentation loads, 100 and 200 g fell into this category, but at loads of 500 g or more nearly 95 % of the tests were acceptable). In most of the successful tests the specimens fractured into four pieces; a representative photograph is shown in Fig. 2. Specimens indented with loads of 500 g or more had cracks emanating from the corners of the indentations. This is probably responsible for the greater proportion of successful tests at the higher loads.

The disks were placed on the lower die with their indented side subjected to biaxial tensile loading. A small amount of vacuum grease was placed on the loading ring and lower die to lubricate the areas of contact with the specimen. This minimizes the lateral forces on the samples during loading. The bending tests were performed as quickly as practically possible after indentation, normally less than 30 minutes. A table model Instron testing machine (Model TM-S-L) with crosshead speed of 8.4  $\mu\text{m/s}$  was used for all the bend tests. The applied force was measured by a 45.4 kg load cell (Interface model SM-100) with an accuracy of 1.8 g (0.01766 N), and the displacement was measured to within 0.06  $\mu\text{m}$  using a linear variable differential transformer (LVDT). The signals from the load cell and the LVDT were collected by an IBM PC with a data acquisition rate of 20 data points per second.

### III. RESULTS

#### A. Measurement of the Fracture Stress, $\sigma_f$

A representative curve of applied load,  $F$ , vs. displacement,  $w$ , is shown in Fig. 3a. The sample in this case was 600  $\mu\text{m}$  thick, indented with a load,  $P$ , of 4.98 N, but the features seen here are independent of these pa-

rameters. The curve is typical in that an initial nonlinear region at the smallest loads and displacements is followed by another region which is linear until the sample fails catastrophically. Immediately after failure the load drops so rapidly that the data acquisition system cannot record it. The maximum load,  $F_m$ , (Fig. 3a) was subsequently used to calculate the fracture stress,  $\sigma_f$ .

A few samples experienced an intermediate drop in load, followed by an increase to even higher loads prior to catastrophic failure. An example of this type of behavior is shown in Fig. 3b. We were unable to uncover any systematic reasons for this behavior; for example, most of the specimens that behaved this way also fractured into four pieces, as in Fig. 2. Apart from this aberration, if the samples exhibiting this behavior were normal in all other respects there was no reason to exclude their values of  $F_m$ , hence they were retained. It is not common practice to determine, or at least report, load-displacement curves in fracture-toughness investigations of ceramics; we are unaware of any published examples. It is possible that the intermediate load drop is associated with the temporary arrest of one of the two cracks, but there is no obvious way of verifying this suggestion.

The fracture stress was calculated from the formula for a thin circular plate of thickness  $t$  subjected to elastic bending under the simply-supported edge boundary condition<sup>9</sup>, namely

$$\sigma_f = \frac{3F_m}{2\pi t^2} \left[ (1 + \nu) \ln \frac{a}{b} + \frac{1 - \nu}{2} \left( 1 - \frac{b^2}{a^2} \right) \right], \quad (1)$$

where  $\nu$  is Poisson's ratio, and  $a$  and  $b$  are the radius of the lower die and the loading ring, respectively. Equation (1) is valid, strictly speaking, for a loading ring with an infinitely thin wall thickness, which is not realized in practice. Therefore, a formula has been derived for the more realistic case of a loading ring with inner and outer radii  $b_1$  and  $b_2$ , respectively, namely

$$\sigma_f = \frac{3F_m}{2\pi t^2} \left\{ 1 + \frac{1}{b_2^2 - b_1^2} \left[ (1 + \nu) \left( b_2^2 \ln \frac{a}{b_2} - b_1^2 \ln \frac{a}{b_1} \right) - \frac{(1 - \nu)(b_2^4 - b_1^4)}{4a^2} \right] \right\}. \quad (2)$$

It turns out that if  $b$  in equation (1) is taken as  $(b_1 + b_2)/2$ , equations (1) and (2) yield almost identical results. The difference between them is less than 0.1% for the test parameters in our experiments, therefore equation (1) was used for all the calculations, with  $b = (b_1 + b_2)/2$ .

## B. Evaluation of the Fracture Toughness

All the data on  $\sigma_f$  as a function of  $P$  are presented in the log-log plot in Fig. 4, where it is evident that  $\sigma_f$  decreases with increasing  $P$ . This type of behavior is representative of ceramics exhibiting R-curve behavior. The basis of R-curve behavior in controlled flaw tests is that the total stress intensity factor,  $K$ , driving crack propagation can be written as<sup>7</sup>

$$K = K(c) = \psi \sigma_a c^{1/2} + \frac{\chi P}{c^{3/2}}, \quad (3)$$

where  $c$  is the crack length,  $\sigma_a$  is the applied stress,  $\psi$  is a dimensionless constant related to the crack geometry and  $\chi$  is an elastic parameter<sup>10</sup> which is given by

$$\chi = 0.004 \left( \frac{E}{H} \right)^{1/2}, \quad (4)$$

where  $E$  is Young's modulus and  $H$  is the Vickers hardness. The first term in equation (3) is due to the applied stress and the second is due to the residual stress associated with the indentation. The description of R-curve behavior is completed by equating (3) to the fracture resistance,  $T$ , which is a function of the crack length, i. e.  $T = T(c)$ . A crack can propagate in an unstable manner as soon as it reaches a critical length,  $c^*$ , defined by the conditions

$$K(c^*) = T(c^*); \quad (5a)$$

$$\left( \frac{dK}{dc} \right)_{c=c^*} = \left( \frac{dT}{dc} \right)_{c=c^*}. \quad (5b)$$

Equation (5a) defines  $T(c^*)$ , the apparent fracture toughness of a material containing a crack of length  $c^*$ . Unstable crack growth in this material occurs when the first term in equation (5b) is greater than the second.

The principal feature that distinguishes the various theoretical treatments of R-curve behavior is the function chosen to represent  $T(c)$ . Perhaps the most common function chosen represents power-law behavior, namely<sup>11-13</sup>

$$T(c) = T_0 \left( \frac{c}{c_0} \right)^n, \quad (6)$$

where  $T_0$ ,  $c_0$  and  $n$  are empirical material constants with no special physical significance except that  $T_0$  and  $c_0$  represent some characteristic toughness and crack length, respectively. A different relationship between  $T(c)$  and  $c$  has been suggested by Cook et al.<sup>14</sup>, namely

$$T(c) = T_\infty - \frac{\mu Q}{c^{3/2}}, \quad (7)$$

where the product  $\mu Q$  represents a "microstructural" driving force and  $T_\infty$  represents the toughness at infinite crack length. Other functional dependencies for  $T(c)$  have been proposed<sup>15</sup>, but they will not be considered further here.

It is not difficult to show using equations (5) (see e. g. the paper by Krause<sup>11</sup>) that the function in equation (6) leads to a power law relationship between  $\sigma_f$  and  $P$  of the form

$$\sigma_f = AP^{-q}, \quad (8)$$

where  $q$  and  $n$  are related by the formula<sup>11</sup>

$$n = \frac{1-3q}{2+2q}. \quad (9)$$

Whereas it is certainly possible to fit a straight line to the data in Fig. 4, we do not believe that the fit is good enough to justify the description of R-curve behavior by equation (6), and have instead chosen to use equation (7) for further analysis.

Cook et al.<sup>14</sup> divide the fracture behavior into two regimes, a "microstructure-controlled" regime in which  $\sigma_f$  is independent of  $P$  but the apparent fracture toughness is not, and an "indentation-controlled" regime in which  $\sigma_f$  varies as  $P^{-1/3}$  while the fracture toughness is independent of  $P$ ; a critical load,  $P^*$ , separates the two regimes. They observed that the strength of numerous ceramics approached the microstructure-controlled regime as the indentation size began to approach the grain size of the material. Using equation (7) in conjunction with equations (5), they showed that  $\sigma_f$  is related to  $T_\infty$  by the equation

$$\sigma_f = \frac{3}{\psi\chi^{1/3}} \left( \frac{T_\infty}{4} \right)^{4/3} \frac{1}{(P + P^*)^{1/3}}, \quad (10)$$

where  $\chi P^* = \mu Q$ . Equation (10) predicts the existence of two regimes of behavior in a plot of  $\log \sigma_f$  vs.  $\log P$ ; at small indentation loads  $\sigma_f$  should approach a constant value, whereas at large loads  $\sigma_f$  should vary as  $P^{-1/3}$ .

We believe that the data in Fig. 5 are more consistent with the predictions of equation (10) than equation (8), with  $\sigma_f$  approaching a constant value at small  $P$  and approaching the predicted  $P^{-1/3}$  dependence at large  $P$ . In previous work<sup>14</sup> the values of  $T_\infty$  and  $P^*$  have been determined by optimizing the fit between equation (10) and the experimental results. However, on rewriting equation (10) as

$$\frac{1}{\sigma_f^3} = \chi \left( \frac{4}{T_\infty} \right)^4 \left( \frac{\psi}{3} \right)^3 (P + P^*), \quad (11)$$

it is apparent that the data should fall on a straight line if plotted in the form  $1/\sigma_f^3$  vs.  $P$ , and that  $T_\infty$  and  $P^*$  are readily obtained from the slope and the intercept of the curve. This method of evaluating the data overcomes

the objection raised by Krause<sup>11</sup> about the need for large-scale crack behavior in the evaluation of  $T_\infty$ .

The data in Fig. 4 are replotted in this way in Fig. 5, where the line drawn is a regression curve obtained by least-squares fitting of the data. To extract the best values of  $T_\infty$  and  $P^*$  from the slope and intercept of the line in Fig. 5, it is necessary to choose the correct value of  $\psi$ . Estimating  $\psi$  is not easy, because this parameter is related to the stress intensity at the crack tip, which for our small samples is very possibly strongly influenced by the geometry of the samples as well as the crack. In the following analysis we use the value  $\psi = 1.24$  in our calculations, as recommended by Cook et al<sup>10</sup>. This choice is justified later.

Using the values of  $H$  measured from the indentations of the disk specimens and  $\psi = 1.24$  in equation (3), the values of  $T_\infty$  and  $P^*$  obtained from the slope and intercept of the fitted line are  $T_\infty = 0.87 \pm 0.08 \text{ MPa}\cdot\text{m}^{1/2}$  and  $P^* = 3.07 \text{ N}$  (these values were also used to calculate the curve in Fig. 4). The great advantage of plotting and analyzing the data in this way is that it is not necessary to make measurements at high loads ( $P > P^*$ ) in order to obtain  $T_\infty$ . This is particularly useful for the MDBFTT, since scaling up the size of the samples is unnecessary.

The value of  $T_\infty = 0.87 \pm 0.08 \text{ MPa}\cdot\text{m}^{1/2}$  is close to that provided by the supplier ( $1.0 \text{ MPa}\cdot\text{m}^{1/2}$ ), determined by the Vickers indentation technique. It is also in good agreement with values obtained by more conventional methods,  $T_\infty = 0.67 \text{ MPa}\cdot\text{m}^{1/2}$  by four-point bending<sup>17</sup> and  $1.0 \text{ MPa}\cdot\text{m}^{1/2}$  obtained using the double torsion technique<sup>18</sup>.

#### IV. DISCUSSION

Having demonstrated that the MDBFTT yields data that can be analyzed to extract a value of  $T_\infty$  that compares favorably with those obtained by other methods, it is important to address the major issue of the effect of specimen size with respect to the flaws introduced by indentation and the geometry of the test apparatus.

There is a minimum acceptable thickness of the specimen in the MDBFTT. Anstis et al.<sup>1</sup> have shown that the thickness of the disks should be much larger than the diameter of the initial crack to eliminate surface effects. Their criterion is  $t > 10 c_0$ , where  $c_0$  is the equilibrium crack length after the indentation. Thus  $t = 10 c_0$  defines the lower limit of the thickness. In principle there is no upper limit to the thickness of a disk specimen for the ring-on-ring test, since the portion of the disk inside the loading ring is in a state of pure bending. However, as the thickness of the specimen is increased the contact stress at the loading ring becomes very large, because the load needed to produce the fracture stress is large. As a practical matter we arbitrarily choose as a criterion a maximum thickness,  $t_m$ , such that the maximum contact stress,  $\sigma_c = F_m/2\pi b\Delta b$ , where  $\Delta b$  is the wall thickness of the loading ring, does not exceed twice the fracture stress. Then, setting  $\sigma_c = 2\sigma_f$ , with  $\sigma_f$  given by equation (1) and  $t = t_m$ , we find on



substituting the parameters relevant to this work that  $t_m = 830 \mu\text{m}$ . This is somewhat greater than the thickest sample we tested ( $700 \mu\text{m}$ ).

The geometry of the sample also affects the values of fracture toughness through the parameter  $\psi$ , which influences the stress intensity factor. To estimate  $\psi$  we used the empirical equation of Newman and Raju<sup>16</sup> to calculate the stress intensity factors of surface cracks as a function of specimen geometry. The ratios  $c^*/t$  and  $c^*/b$ , as well as  $\phi$ , where  $\phi$  is the angle between the surface of the specimen and the crack front (measured from the mid-point of the crack), all affect the stress intensity factor\*. In our tests the effect of  $c^*/b$  is small because  $b \gg c^*$ . If we assume that the crack retains its semicircular shape during propagation and assign a single value of the stress intensity factor along the crack front, then the equations of Newman and Raju can be used to calculate the stress intensity factor as a unique function of  $c^*/t$ .

The necessary calculations were performed by computer to calculate the value of  $\psi$  relevant to the parameters characteristic of our tests. The required estimates of  $c^*$  were calculated using the formula<sup>14</sup>

$$c^* = \left[ \frac{\chi(P+P^*)}{T_\infty} \right]^{2/3}, \quad (12)$$

in conjunction with the experimentally determined values of  $P^*$  and  $T_\infty$ . For the range of  $c^*/t$  in our tests, namely 0.11 to 0.33, the corresponding values of  $\psi$  decrease from 1.25 to 1.16. Since the smaller values of  $c^*/t$ , hence the larger values of  $\psi$ , obtain at the smaller loads, it is possible that there is a small contribution of sample geometry to the observed R-curve behavior. Its contribution would not appear to be significant, however, because if we use the average value  $\psi = 1.205$  to calculate  $T_\infty$ , the result is  $T_\infty = 0.85 \text{ MPa}\cdot\text{m}^{1/2}$ , which differs by only 3% from the value obtained using  $\psi = 1.24$ .

For conventional fracture-toughness tests on plate-shaped specimens the thickness and crack width are identical, and the thickness should be much larger than the size of the plastic zone at the crack tip to assure plane strain conditions. In normal bend tests on pre-indented large ceramic samples the initial and critical crack sizes are ordinarily so much smaller than the thicknesses of the specimens that adjusting the size of the specimens to accommodate the larger flaws produced by high indentation loads is unnecessary. For example, in Krause's experiments<sup>11</sup>, the ratio of crack size to specimen thickness varied by about an order of magnitude (0.02 to 0.20), yet  $\psi$  decreased by only 6.7% (from 1.20 to 1.12). In the MDBFTT the dependence of  $\psi$  on  $c^*/t$  is more sensitive than this, with  $\psi$  decreasing by

---

\*The stress intensity factor along the crack front is not constant, and is higher at regions of the crack tip near the specimen surface. This will affect the shape of the crack as discussed by Krause<sup>11</sup>.

7.2% as  $c^*/t$  increases by a factor of three. This suggests that the thicknesses of the samples in the MDBFTT have to be chosen rather more carefully than in bending tests on large samples, and that a criterion for making the correct choices would be useful.

We suggest as an appropriate criterion that the ratio of critical crack length to the sample thickness should be maintained nearly constant to eliminate specimen size effects on the experimental value of  $T_\infty$ . Since the critical crack length,  $c^\dagger$ , is not known beforehand, our suggestion would not appear to be very helpful in designing experiments\*\*. However, it has been reported that  $c^\dagger$  is proportional to  $c_0$  and the ratio of these two lengths is independent of the indentation load<sup>14</sup>. Since  $c_0$  is a function of  $P$  through the established equations of indentation toughness measurements<sup>1</sup>, we can write

$$c_0 = \left( \frac{\chi}{T_\infty} \right)^{2/3} P^{2/3} = \beta c^\dagger, \quad (13)$$

where  $\beta$  is a proportionality constant. To maintain the ratio  $c^\dagger/t$  constant for two specimens with indentation loads  $P_1$  and  $P_2$ , the relation between the thicknesses of the two samples should be

$$\frac{t_1}{t_2} = \frac{c_1^\dagger}{c_2^\dagger} = \left( \frac{P_1}{P_2} \right)^{2/3}. \quad (14)$$

Equation (14) provides the criterion we seek because it specifies the relationship between  $t$  and  $P$  required to maintain  $c^\dagger/t$  constant without needing to know anything about the fracture behavior of the material. This criterion, in conjunction with  $t > 10 c_0$ , should serve as valuable guidelines for the preparation of specimens for the MDBFTT.

Finally, we address the issue of the geometrical parameters used in the test apparatus, because these can also influence the results. The ratio of the diameters of the lower die (2a) and the loading ring (2b) is the most important factor here. If  $b/a$  is too small the contact stress exerted on the specimen by the loading ring, and vice versa, can exceed the yield stresses of either the loading ring or the specimen. On the other hand, from practical considerations the inner diameter of the loading ring should be larger than the length of the initial crack length, i. e.  $b \gg c_0$ . This ensures that the area over which the stress is constant is as large as possible. However, the value of  $b/a$  does have an upper limit because  $\sigma_f$  becomes zero as  $b/a$  approaches unity, as can be seen from equation (1). It does not seem possible to determine an optimum value of  $b/a$ , but as a working hypothesis we

---

\*\*The crack lengths  $c^*$  and  $c^\dagger$  are not necessarily identical. The former is calculated, in our case using equation (12), whereas the latter is intended to represent the actual critical crack length in the specimen.

suggest that if  $b/a$  satisfies the condition  $0.3 < b/a < 0.7$  the accuracy and sensitivity of the test is assured;  $b/a = 0.45$  in our apparatus.

## V. CONCLUSIONS

1. It has been demonstrated that the fracture toughness of a ceramic material can be measured successfully by the MDBFTT. Experiments on CVD-grown ZnS yield the fracture toughness  $T_{\infty} = 0.87 \pm 0.08 \text{ MPa}\cdot\text{m}^{1/2}$ , which is in good agreement with the values obtained by the bend testing of large specimens, and by the indentation toughness method.

2. The data on ZnS exhibit R-curve behavior. The equations of Cook et al.<sup>14</sup> accurately describe the relationship between fracture stress and indentation load. A graphical procedure has been developed to analyze the data using the equations of Cook et al., which has the advantage that data at large indentation loads are not required to extract the correct value of  $T_{\infty}$ .

3. A criterion for selecting the thicknesses of samples in the MDBFTT is proposed. As the  $P$  increases,  $t$  should be increased as  $P^{2/3}$ . This assures that the stress intensity at the front of a crack of critical size is independent of the thickness of the specimens. As demonstrated by our results, small departures from this criterion do not seriously affect the values of  $T_{\infty}$ .

## ACKNOWLEDGEMENTS

The authors are grateful to the Office of Naval Research for financial support this research under Contract No. N00014-87-K-0531. Funding for the construction of the test apparatus was provided by the Department of Energy under grant no. DE-FG03-86 ER45264. Felix C. Chen provided invaluable instruction in the use of the test facility, and his help is greatly appreciated.

## REFERENCES

1. G. R. Anstis, P. Chantikul, B. R. Lawn and D. B. Marshall, *J. Am. Ceram. Soc.*, **64**, 533 (1981).
2. G. E. Lucas, *Metall. Trans.*, **21A**, 1105 (1990).
3. H. Li, F. C. Chen and A. J. Ardell, submitted to *Metall. Trans. A* for publication (1990).
4. J. Zhang, W. W. Chen and A. J. Ardell, presented at the International Symposium on Optical and Optoelectronic Applied Science and Engineering, Window and Dome Technologies and Materials II, SPIE Proc., **1326**, San Diego, California, USA, 1990. To be published.
5. J. Zhang, W. W. Chen, A. J. Ardell and B. Dunn, *J. Am. Ceram. Soc.*, **73**, 1544 (1990).
6. J. Zhang, W. W. Chen, B. Dunn and A. J. Ardell, in *Ceramics and Inorganic Crystals for Optics, Electro-Optics, and Nonlinear Conversion*, edited by R. W. Schwartz (SPIE Proc., **968**, 1988) p. 35.
7. P. Chantikul, G. R. Anstis, B. R. Lawn and D. B. Marshall, *J. Am. Ceram. Soc.*, **64**, 539 (1981).

8. D. C. Harris, W. R. Compton, A. M. Harper, G. A. Hayes, M. E. Hills, N. A. Jaeger, L. D. Sawyer, R. C. Scheri and J. L. Stokes, presented at the International Symposium on Optical and Optoelectronic Applied Science and Engineering, Window and Dome Technologies and Materials II, SPIE Proc., 1326, San Diego, California, USA, 1990. To be published.
9. R. J. Roarke and W. C. Young, *Formulas for Stress and Strain* (McGraw-Hill Book Company, New York, 1975), 5th ed. p. 382.
10. R. F. Cook, C. J. Fairbanks, B. R. Lawn and Y.-W. Mai, *J. Mater. Res.* 2, 345 (1987).
11. R. F. Krause, Jr., *J. Am. Ceram. Soc.*, 71, 338 (1988).
12. D. K. Shetty and J.-S. Wang, *J. Am. Ceram. Soc.*, 72, 1158 (1989).
13. R. F. Cook and D. R. Clarke, *Acta Metall.*, 36, 555 (1988).
14. R. F. Cook, B. R. Lawn and C. J. Fairbanks, *J. Am. Ceram. Soc.*, 68, 604 (1985).
15. A. G. Evans, in *Advances in Ceramics, Science and Technology of Zirconia II*, 12, edited by N. Claussen, M. Rühle and A. H. Heuer (American Ceramic Society, Columbus, OH, 1984), p. 193.
16. J. C. Newman, Jr. and I. S. Raju, *Engr. Fract. Mech.*, 15, 185 (1981).
17. W. F. Adler and S. V. Hooker, *J. Mater. Sci.*, 13, 1015 (1978).
18. D. P. Williams and A. G. Evans, *J. Test. and Eval.*, 1, 264 (1973).

Table 1. Physical Properties of the CVD-Grown ZnS used in this investigation.

Grain Size ( $\mu\text{m}$ )	Hardness (GPa)	Flexural Strength (MPa)	Young's Modulus (GPa)	Poisson's Ratio	Fracture Toughness ( $\text{MN}\cdot\text{m}^{1/2}$ )
20-35	1.5	50-60	74.5	0.28	1.0

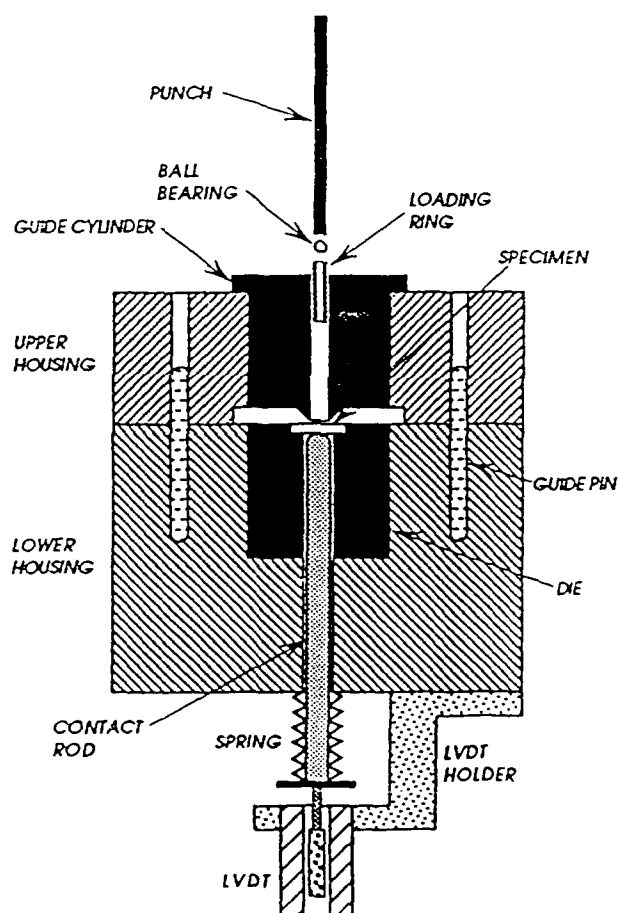


Fig. 1. Schematic diagram of the apparatus used for the miniaturized disk bend fracture toughness tests.



Fig. 2. Photograph of the pieces of a 700  $\mu\text{m}$  thick sample of ZnS after fracture. The indentation load was 19.6 N.

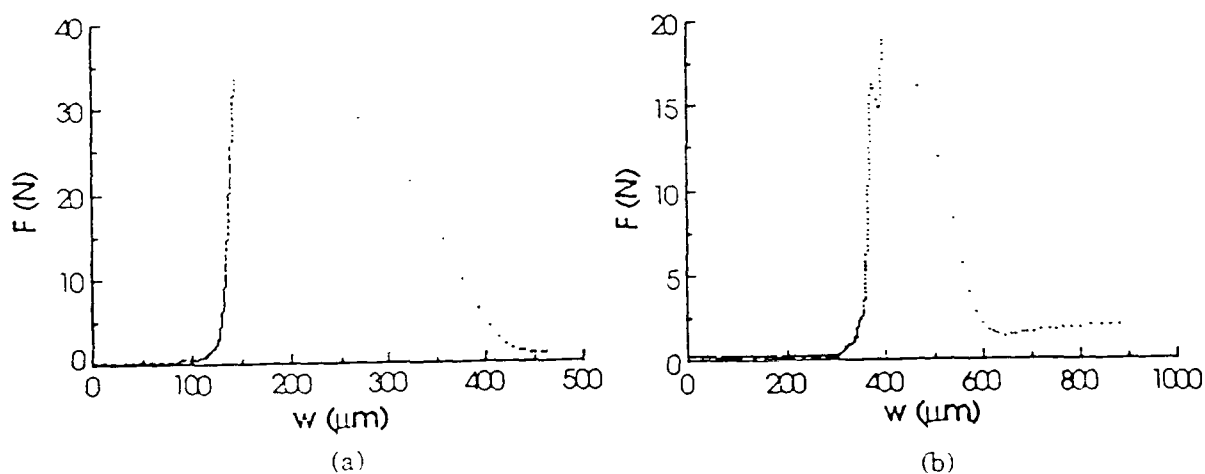


Fig. 3. Curves of applied load,  $F$ , vs. displacement,  $w$ , for two specimens indented with a load of 4.9 N. The curve in (a), for a sample 570  $\mu\text{m}$  thick, was typical of that obtained for most of the specimens. The curve in (b), for a sample 560  $\mu\text{m}$  thick, exhibited intermediate unloading before fracture.

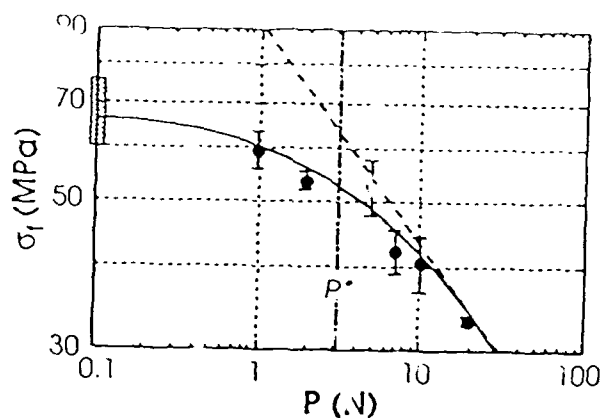


Fig. 4 A log-log plot of fracture stress,  $\sigma_f$ , vs. indentation load,  $P$ . The shaded rectangle indicates the values of  $\sigma_f$  for the unindented specimens. The value of  $P^*$  and the solid curve were derived from analysis of the data, as described in the text. The slope of the dashed line is  $-1/3$ .

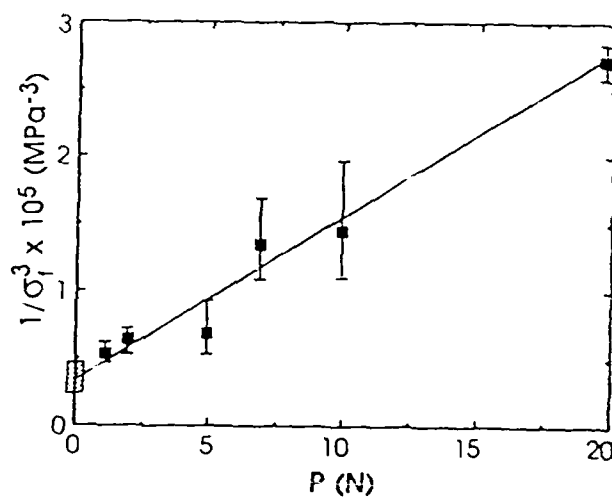


Fig. 5 The data in Fig. 4 replotted in the form  $(1/\sigma_f)^3$  vs.  $P$ . The shaded rectangle at  $P = 0$  represents the data on unindented samples; these were not included in the least-squares fit used to obtain the straight line shown.

## Experimental and Theoretical Studies of Second-phase Scattering in IR Transmitting ZnS-based Window

William W. Chen, B. Dunn, J. M. Zhang

Department of Materials Science and Engineering  
University of California, Los Angeles, CA 90024, U. S. A.

### ABSTRACT

A model based upon Mie theory was developed to calculate the level of scattering caused by the incorporation of a second-phase. Various transmission curves were calculated in order to study the microstructural scattering effects of pores and  $\text{ZnGa}_2\text{S}_4$  particles. The model was able to reproduce the spectral transmission curve (2.5 - 10  $\mu\text{m}$ ) of a hot-pressed ZnS sample containing a porous scatterer only when a size distribution effect was included in the model. A bimodal distribution of pores was found to be responsible for the detected scattering.

### 1. INTRODUCTION

The design of a multiphase ZnS-based ceramic window is influenced by a compromise between mechanical and optical considerations. This process seeks to optimize the strength and fracture toughness of the window while minimizing the scattering due to the second-phase. From an optical viewpoint, a single-phase material with a cubic crystal structure is best suited as a window material because the anisotropic and second-phase scattering mechanisms are intrinsically absent. However, the motivation to develop a multiphase or composite ZnS-based window is to improve its mechanical properties beyond those of the single-phase material. The approach for the design of such a window and some mechanical property measurements has been discussed previously.<sup>1</sup> There is usually an optimum value of parameters such as the volume fraction, size and size distribution that results in the best mechanical properties. Unfortunately, the features which characterize the dispersion of the second-phase are not necessarily the most suitable ones for optical transmission.

Since the optical scattering is very sensitive to the characteristics of the dispersion of scatterer, it is important to be able to understand the influences of each second-phase parameter upon the optical transmission of the window. The present study has used Mie theory as the basis for an optical scattering model. The model enables the calculation of the spectral in-line transmission of 2.5 - 10  $\mu\text{m}$  radiation through a ZnS matrix while varying the characteristics of the dispersion before the window is fabricated. The application of this model will help determine the microstructural features that minimize the scattering loss from a second-phase.

### 2. THEORETICAL BACKGROUND

Figure 1 is a schematic of the various losses in intensity suffered by an incident parallel beam ( $I_0$ ) when it traverses a matrix containing a dispersion of spherical particles. The ratio of the detected intensity ( $I$ ) over the incident intensity is the in-line transmission ( $T$ ) and is described by the following equation:

$$T = \frac{I}{I_0} = (1 - R)^2 \exp(-\gamma t) \quad (1)$$

where  $R$ ,  $\gamma$ , and  $t$  are the reflectivity, attenuation or extinction coefficient and thickness of the sample, respectively. The pre-exponential term accounts for the loss due to two fresnel reflections (one entering



and one exiting the slab) for an uncoated sample. The reflectivity is determined from the refractive index by use of the following equation:

$$R = \frac{(n - 1)^2}{(n + 1)^2} \quad (2)$$

The wavelength dependence of the refractive index must be known in order to calculate the spectral reflectivity. For polycrystalline, cubic ZnS, the refractive index is approximately 2.25 over the wavelength range 2.5 - 10  $\mu\text{m}$ .<sup>2</sup> By the substitution of the value 2.25 into equation 2 and by assuming that the extinction coefficient is zero, the transmission from Equation (1) is calculated to be about 72%.

The extinction coefficient is related to the number of particles per unit volume ( $N_o$ ) in the matrix by:<sup>3</sup>

$$\gamma = N_o C_{\text{scat}} \quad (3)$$

where  $C_{\text{scat}}$  is the scattering cross-sectional area of a single particle. When this quantity is divided by the geometric area ( $\pi r^2$ ), the dimensionless quantity  $Q_{\text{scat}}$ , the scattering efficiency coefficient, is obtained. The extinction coefficient, defined in terms of  $Q_{\text{scat}}$  is given by:<sup>3</sup>

$$\gamma = \frac{3}{4} \frac{V}{r} Q_{\text{scat}} \quad (4)$$

where  $V$  is the volume fraction of the second-phase. An examination of Equation (4) indicates that the spectral  $Q_{\text{scat}}$  curve must be computed in order to calculate the transmission.

Rayleigh<sup>4</sup> derived an expression for the calculation of  $Q_{\text{scat}}$  in terms of a size parameter ( $\alpha$ ) and the relative refractive index ( $n$ ) for the scattering of electromagnetic radiation by small, dielectric spheres. This scattering is based upon the condition that the electric field within the sphere is uniform and parallel to the external field when illuminated by polarized radiation. If the incident field oscillates harmonically, the particle can be considered an oscillating dipole that radiates scattered waves in all direction. For a Rayleigh scatterer dispersed in air, the scattering efficiency factor is

$$Q_{\text{scat}} = \frac{8}{3} \alpha^4 \left( \frac{n^2 - 1}{n^2 + 1} \right)^2 \quad (5)$$

The size parameter is described by ( $2\pi r/\lambda$ ), and the relative refractive index is ( $n_1/n_2$ ) where  $n_1$  and  $n_2$  are the particle and matrix refractive indices, respectively. Equation (5), however, is only valid when the upper limit of the particle size to wavelength ratio ( $r/\lambda$ ) is less than or equal to 0.05. For 2  $\mu\text{m}$  radiation, particles of 0.1  $\mu\text{m}$  radius or smaller are considered Rayleigh scatterers, and in that region, the transmission curve exhibits a characteristic  $\lambda^{-4}$  dependence derived from the quantity  $\alpha^4$  in Equation (5).

The sizes of the second-phase particles in ceramic bodies, however, are not always small with respect to the incident radiation. The scattering of an electromagnetic wave by a homogeneous sphere of arbitrary size is derived from the solution of Maxwell's equations with appropriate boundary conditions. Mie had derived the solution for this type of scattering, and the scattering efficiency coefficient is given as an infinite series of Legendre polynomials whose coefficients are complicated functions of Bessel functions. The Mie formula gives:<sup>5</sup>

$$Q_{\text{scat}} = \frac{2}{\alpha^2} \sum_{k=1}^N (2k + 1) (|a_k|^2 + |b_k|^2) \quad (6)$$

where  $a_k$  and  $b_k$  are the Mie coefficients and are functions of the relative refractive index and size parameter.

The scattering efficiency factor may be calculated for given values of  $n$ ,  $\alpha$ , and  $\lambda$  by adding the terms from Equation (6) in series. The basic problem involved in Mie theory is the evaluation of the

coefficients  $a_k$  and  $b_k$ . Many mathematical methods<sup>6</sup> are available to determine or approximate the Mie coefficients, but most evaluations are now done numerically with the aid of a computer;<sup>7,8</sup> the summation converges to the  $Q_{\text{scat}}$  value after the addition of a certain number of terms. For this study, the spectral scattering efficiency coefficient is calculated numerically. Sample calculations of  $Q_{\text{scat}}$  were compared with prior studies involving systems using air and water as the matrix material. A comparison of the calculated values of the present study and the literature  $Q_{\text{scat}}$  values<sup>9</sup> indicated no discrepancies.

### 3. EXPERIMENTAL

High density ZnS disks were fabricated by uniaxial hot-pressing. The details of the procedure is described elsewhere.<sup>10</sup> The sample was optically polished using a final polishing medium of 0.05  $\mu\text{m}$  alumina. The density of the sample was determined by the water immersion method, and the infrared transmission data was collected with use of a Perkin-Elmer FTIR spectrophotometer.

### 4. CALCULATED TRANSMISSION CURVES FOR SINGLE SIZE SCATTERER

The parameters which affect the scattering characteristic of the two-phase window are evident from equation (4). Two factors to consider are the thickness of the sample and the volume fraction of the scatterer. They are wavelength independent which means that increasing or decreasing these quantities only shifts the transmission level higher or lower, but does not change the shape of the transmission curve.

The scattering efficiency coefficient is wavelength dependent and is a function of the size parameter and the relative refractive index. The amount of scattering depends upon the index mismatch between the matrix and the scatterer and also upon the relative size of the scatterer with respect to the wavelength of the incident radiation.

Transmission curves were calculated in order to observe the influence of each parameter upon the scattering. In each of the figures, a series of curves are plotted which represent the transmission when varying the value of one of the parameters. The effect of volume fraction, size of the scatterer and the type of second-phase are examined over spectral range 2.5 - 10  $\mu\text{m}$ .

Figures 2 and 3 show the calculated transmission curves of a ZnS matrix containing porosity as a second-phase. A pore ( $n_1 = 1$ ) was chosen as the scatterer because it is a very common microstructural feature in ceramic bodies. Figure 2 is a plot of the transmission of 99, 99.5, 99.95 and 99.99% dense 2 mm thick ZnS slabs containing 0.3  $\mu\text{m}$  pores. The calculated curves indicate that for window applications, bulk ZnS pieces must be fabricated so that the volume fraction of voids is reduced to at least  $1 \times 10^{-4}$ . This illustrates the reason why it is often difficult to fabricate optical quality windows by conventional sintering or hot-pressing methods since a very small amount of residual porosity will adversely degrade the transmission. 99.99% dense ZnS window will scatter about 20% at 2.5  $\mu\text{m}$ . Even an increase of an extremely small amount,  $4 \times 10^{-4}$  volume fraction, of the porous phase to 99.95% density will significantly decrease transmission in the 2.5 - 5  $\mu\text{m}$  range (15% transmission @ 2.5  $\mu\text{m}$ ). To determine the transmission curves as function of pore size, the density and sample thickness are fixed at 99.5% and 2 mm, respectively. Figure 3 shows that scattering losses are much lower for smaller size pores and that only pores smaller than 1000  $\text{\AA}$  are essentially homogeneous to 2.5 to 10  $\mu\text{m}$  radiation.

A porous phase in a ceramic piece is an inherently undesirable characteristic because it acts as a stress concentrator thus degrading the intrinsic strength of the sample. On the other hand, the controlled incorporation of  $\text{ZnGa}_2\text{S}_4$  precipitated into a fully dense ZnS matrix is of interest due to the possible

improvement of the mechanical properties of the two-phase material over the pure one.<sup>10</sup> The modelling of the transmission curve for hypothetical ZnS-based windows containing different characteristic ensembles of  $\text{ZnGa}_2\text{S}_4$  precipitates would facilitate the determination of the critical volume fraction and size necessary to achieve a useful transmission property.

There is no refractive index data for  $\text{ZnGa}_2\text{S}_4$  in the literature, however, the refractive index of an analogous compound, a  $\text{ZnIn}_2\text{S}_4$  single crystal, has been measured from 0.6 to 1.25  $\mu\text{m}$ .<sup>11</sup> The dispersion of its refractive index as the IR region is approached is small, and this study has extrapolated the  $\text{ZnIn}_2\text{S}_4$  dispersion curve in the 2.5 - 10  $\mu\text{m}$  range. An examination of the extrapolated curve indicates that a refractive index of 2.5 is a good value for use in the model. This value represents the worst case refractive index because the index of  $\text{ZnGa}_2\text{S}_4$  should be smaller since the polarizability of the  $\text{Ga}^{3+}$  ion is smaller than the  $\text{In}^{3+}$  ion.

Figure 4 is a plot of transmission versus wavelength of a 2 mm thick ZnS-based ceramic containing 500 Å size  $\text{ZnGa}_2\text{S}_4$  precipitates as a function of volume fraction. This size of second phase particles is not uncommon for other systems which are exploited for their precipitation strengthening and hardening effects.<sup>12</sup> The scattering increases as the volume fraction of the second-phase increases, however, most of the scattering is limited to the 2.5 to 4  $\mu\text{m}$  range, and even with 5% volume fraction of precipitates the transmission is only reduced to 64% at 2.5  $\mu\text{m}$ . The transmission curves for a 2 mm thick ZnS ceramic matrix containing fixed 5% volume fraction of different size zinc thiogallate are plotted versus wavelength in figure 5. Similar manner to the behavior of pore scatterer, the transmission decreases as the size of the  $\text{ZnGa}_2\text{S}_4$  precipitate increases. The plot reveals that 5% volume fraction of 250 Å radius particles is virtually transparent to 2.5 to 10  $\mu\text{m}$  radiation. A comparison of the hypothetical 0.1  $\mu\text{m}$  size zinc thiogallate and pore (Figures 3 and 5) indicates that the porous sample scatters less despite the fact that the absolute value of the refractive index mismatch ( $\Delta n$ ) for the pore is much greater than that of the  $\text{ZnGa}_2\text{S}_4$ . We also see that the number of scatterers is the dominant influence upon the scattering characteristic of these two transmission curves because the porous sample contains an order of magnitude fewer scatterers.

There are still many combinations of relative refractive index, volume fraction and size of the scatterer for which the transmission curves have yet to be calculated. By the use of the model, we have seen that with all else being equal, the scattering decreases as the refractive index mismatch, the volume fraction second-phase, and the size of the scatterer decreases. However, with the proper combination of each parameter, it is possible to tailor a two-phase microstructure for ZnS which is transparent to 2.5 to 10  $\mu\text{m}$  radiation.

## 5. EXPERIMENTAL RESULTS AND ANALYSIS

### 5.1. Fully dense samples and single pore size scattering

The infrared transmission for a 2.1 mm thick hot-pressed ZnS and of IRTRAN 2, a commercially available hot-pressed ZnS window, are plotted in figure 6. The IRTRAN 2 sample exhibits near theoretical transmission accounting for two fresnel reflections at the surfaces. This behavior indicates that  $\gamma$  is zero and that the material is fully dense (> 99.99%). The measured densities of the hot-pressed ZnS (30,000 psi pressure) and the IRTRAN 2 samples are 99.74 and 99.77%, respectively, based upon the x-ray density whose lattice parameter is 5.406 Å.<sup>13</sup> The corrected density of our hot-pressed sample is 99.964%. Addition of the correction factor to the IRTRAN 2 measured density would make its density consistent with the infrared transmission data.

The transmission data for the hot-pressed ZnS sample (30,000 psi pressure) was analyzed by the scattering model in an attempt to derive the size of the pore and thus test the validity of the model. However, it was not possible, based upon the model and the experimental data to determine a pore size since none of the calculated transmission curves fitted well with the measured one. This inconsistency revealed that the assumption of a single size scatterer for real systems was invalid, and therefore a function describing the size distribution of the scatterer needs to be incorporated into the model.

## 5.2. Polydispersity modification and experimental curve fitting

The number of particles per unit volume is not a constant anymore but is now a function of the radius ( $N(r) = N_0 f(r)$ ). Modification of Equation (4) based upon this new assumption gives:

$$\gamma = \frac{3}{4} V \left\{ \int_{r_0}^{r_1} f(r) Q_{sca} r^2 dr / \int_{r_0}^{r_1} f(r) r^3 dr \right\} \quad (7)$$

where  $r_1$  and  $r_0$  are the upper and lower limits of the size distribution function ( $f(r)$ ). The extinction coefficient now describes the scattering due to an ensemble of scatterers whose size is described by  $f(r)$ .

An iterative process was used to fit the experimental transmission data to the one generated by the model. The  $f(r)$  used for the fitting was a zeroth-order lognormal distribution (ZOLD) function that is characterized by two parameters, the modal radius and width ( $r_m$  and  $\sigma$ ).<sup>13</sup> It was found that a bimodal ZOLD distribution generated a transmission curve illustrated in figure 7 using the appropriate experimental sample thickness and volume fraction. The bimodal distribution is plotted semi-logarithmically in figure 8. There is rather good agreement between the calculated curve and the experimental transmission data points.

## 6. SUMMARY

An optical model based upon Mie theory was developed to study the microstructural influences upon the 2.5 - 10  $\mu$ m infrared transmission of ZnS-based ceramics. It was found that the scattering losses are minimized as the refractive index mismatch, volume fraction second-phase and size of the scatterer is decreased, however, the model based upon the use of a single size scatterer was unable to calculate a transmission curve which fitted with the experimental transmission curve of a ZnS sample containing porous scatterer. A model which incorporates the size dispersion effect of the scatterer was able to generate a transmission curve that matches the experimental results. The agreement between the experimental and calculated curves indicates that it is now possible model to predict the transmission behavior for ZnS-based ceramics prior to fabrication of the window.

## 7. ACKNOWLEDGEMENT

The authors are grateful to the Office of Naval Research No. N00014-87-K-0531, for their financial support of this work. The authors wish to thank Professor A. J. Ardell for his help during this entire investigation.

## 8. REFERENCES

1. J. M. Zhang, W. W. Chen, B. Dunn, A. J. Ardell, "Phase diagram studies of ZnS systems", pp. 35-40 in Proceedings of SPIE--The International Society for Optical Engineering, 968, Ceramics and

- Inorganic Crystals for Optics, Electro-Optics, and Nonlinear Conversion, Edited by R. W. Schwartz, Society for Photo-Instrumentation Engineerings, Bellingham, WA (1988).
2. H. H. Li, "Refractive Index of ZnS, ZnSe, and ZnTe and Its Wavelength and Temperature Derivatives", *J. Phys. Chem. Ref. Data* **13**, 103-150 (1984).
  3. L. P. Bayvel and A. R. Jones, Electromagnetic Scattering And Its Applications, Applied Science Publishers, Inc., London and New Jersey (1981).
  4. H. C. Van de Hulst, Light Scattering by Small Particles, John Wiley & Son, New York (1957).
  5. J. A. Stratton, Electromagnetic Theory, McGraw-Hill Book Company, Inc., New York (1941).
  6. M. Kerker, The Scattering of Light and Other Electromagnetic Radiation, Academic Press, New York (1969).
  7. J. V. Dave, "Scattering of Electromagnetic Radiation by a Large Absorbing Sphere", *IBM J. Res. Develop.* **13**, 302-313 (1969).
  8. W. J. Wiscombe, "Improved Mie scattering algorithms", *Appl. Opt.* **19**, 1505-1509 (1980).
  9. N. C. Wickramasinghe, Light Scattering Functions for Small Particles with Applications in Astronomy, John Wiley & Son, New York, NY (1973).
  10. Jimin Zhang, W. W. Chen and A. J. Ardell, "Solid Solution Strengthening of ZnS", pp. 93-98 in Proceedings of SPIE--The International Society for Optical Engineering, **1326**, Window and Dome Technologies and Materials II, Edited by Paul Klocek, Society for Photo-Instrumentation Engineers, Bellingham, WA (1990).
  11. Anneda, "Refractive Index Determination of Layered Compound  $\text{ZnIn}_2\text{S}_4$ ", *Appl. Opt.* **13**, 1595-1598 (1974).
  12. E. W. Kruse II and M. E. Fine, "Precipitation Strengthening of MgO by  $\text{MgFe}_2\text{O}_4$ ", *J. Am. Cer. Soc.* **55**, 32-37 (1972).
  13. ASTM X-ray card 5-0492.
  14. W. F. Espenscheid, M. Kerker, and E. Matijevic, "Logarithmic Distribution Functions for Colloidal Particles", *The J. of Phys. Chem.* **68**, 3093- 3097 (1964).

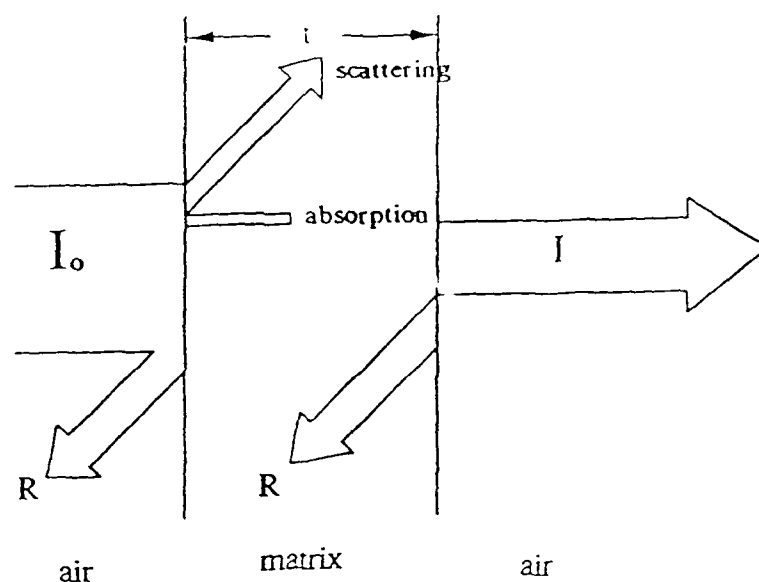


Fig. 1. Schematic of loss mechanisms upon an incident radiation of intensity  $I_0$  where  $R$  and  $I$  are the fresnel reflection loss and the transmitted in-line intensity, respectively

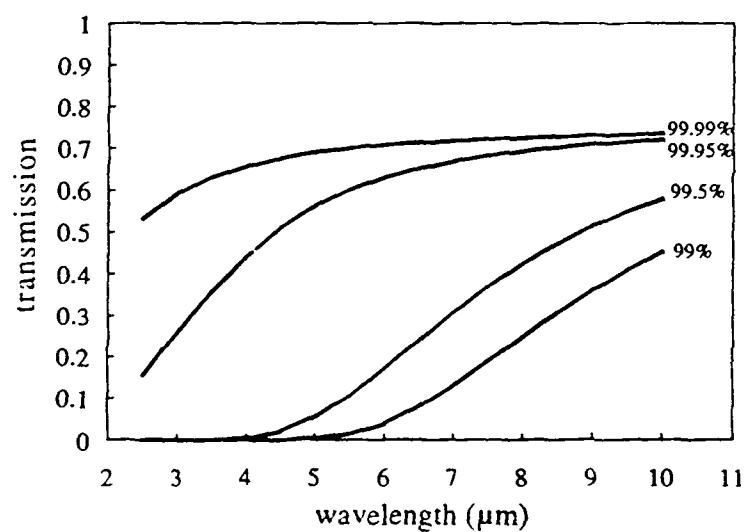


Fig. 2. Transmission curves of hypothetical 2 mm thick ZnS parallel slab containing  $0.3 \mu\text{m}$  pore as a function of volume fraction porosity

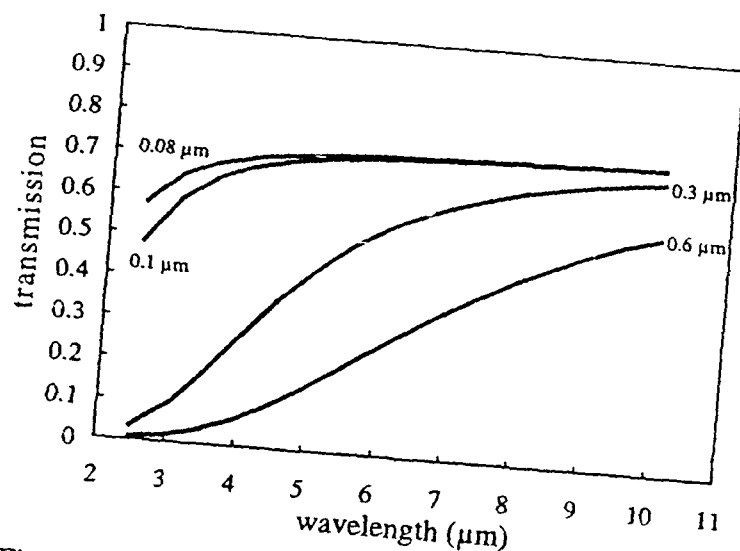


Fig. 3. Transmission curves of hypothetical 2 mm thick ZnS parallel slab containing a fix  $5 \times 10^{-3}$  volume fraction of porous phase as a function of pore size

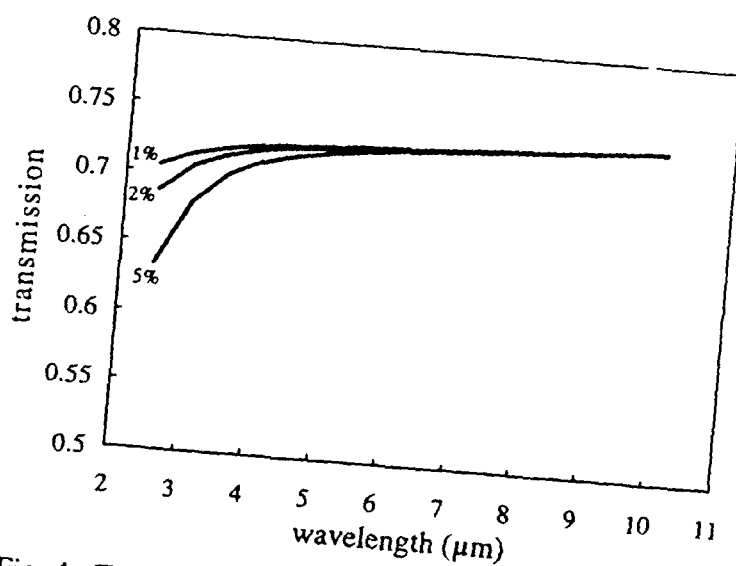


Fig. 4. Transmission curves of a hypothetical 2 mm thick ZnS parallel slab containing 500 Å radius  $\text{ZnGa}_2\text{S}_4$  particles as a function of % volume fraction

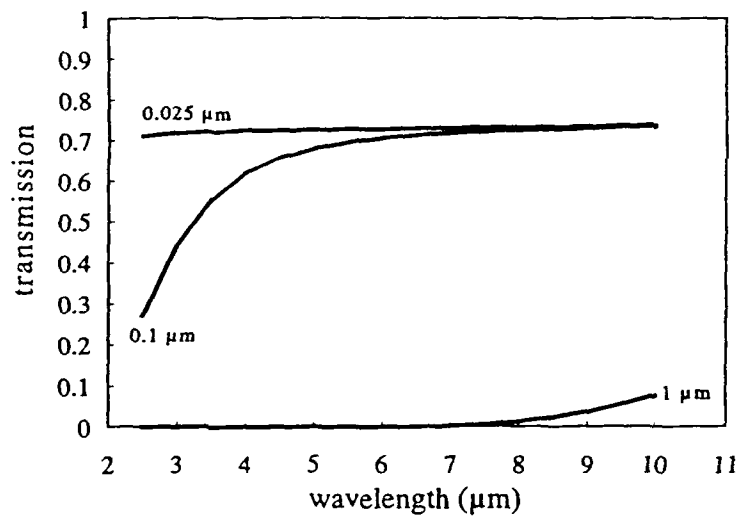


Fig. 5. Transmission curves of a hypothetical 2 mm thick ZnS parallel slab containing a fixed 5% volume fraction of different size  $\text{ZnGa}_2\text{S}_4$  particles

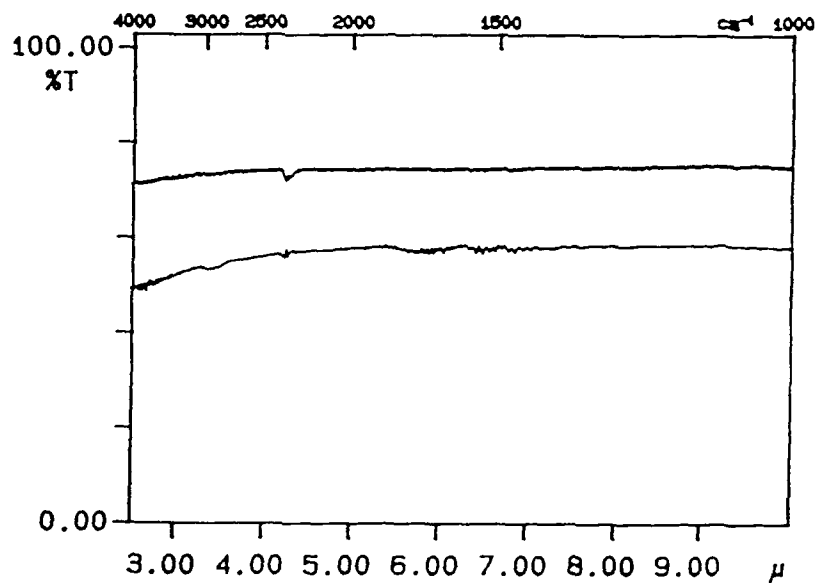


Fig. 6. Experimental transmission curves of Irtran 2 and of a 2.1 mm thick hot-pressed ZnS disk



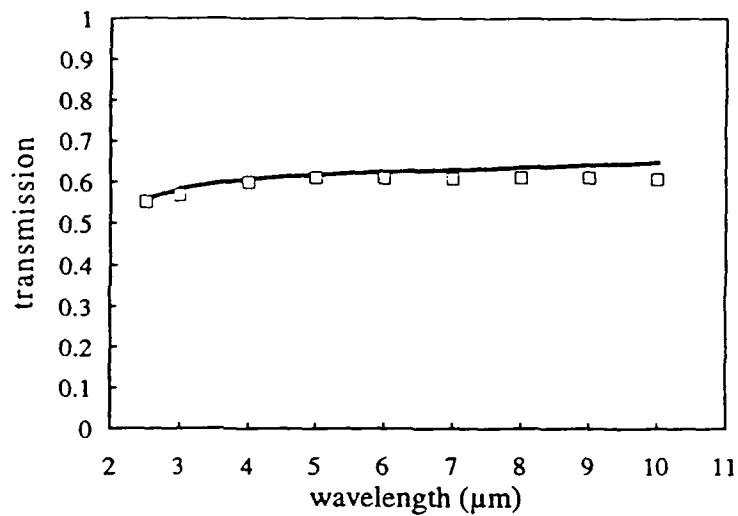


Fig. 7. The experimental transmission curve of 2.1 mm thick ZnS disk hot-pressed at 30,000 psi is indicated by the square data points. The solid line represent a transmission curve generated to fit the experimental data based upon a pore distribution plotted in fig. 8.

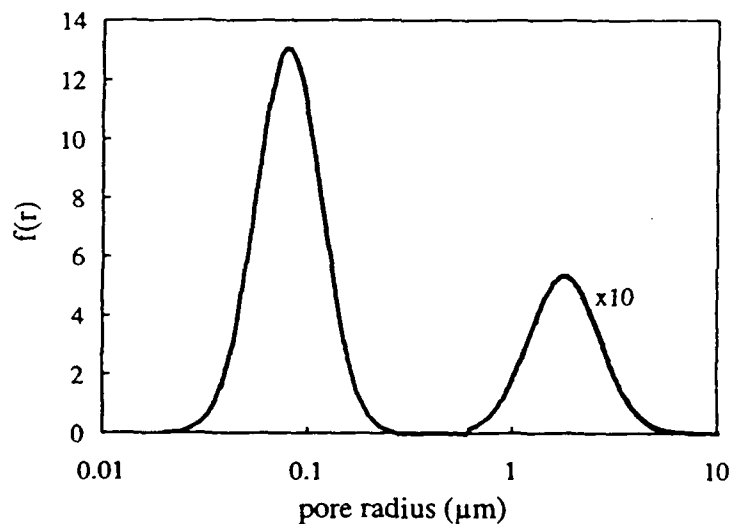


Fig. 8. Semi-logarithmic plot of a bimodal ZOLD function versus pore radius. The modal radii are 0.08 and 1.8  $\mu\text{m}$ , and the widths of the distribution ( $\sigma$ ) are 0.38 and 0.4 respectively.